Mon. Not. R. Astron. Soc. **000**, 000–000 (0000) Printed 15 January 1997 (MN LaTeX style file v1.3)

A study of FRII radio galaxies with $z < 0.15$ – II. High-resolution maps of eleven sources at 3.6 cm

J. P. Leahy[1], A. R. S. Black[2] ⋆, J. Dennett-Thorpe[2], M. J. Hardcastle[2], S. Komissarov[1,3], R. A. Perley[4], J. M. Riley[2] and P. A. G. Scheuer[2]

[1] *Nuffield Radio Astronomy Laboratories, Jodrell Bank, Macclesfield, Cheshire, SK11 9DL*
[2] *Mullard Radio Astronomy Observatory, Cavendish Laboratory, Madingley Road, Cambridge, CB3 0HE*
[3] *Department of Applied Mathematical Studies, University of Leeds, Leeds LS2 9JT*
[4] *National Radio Astronomy Observatory, Socorro, New Mexico, U.S.A.*

15 January 1997

ABSTRACT

VLA maps of total intensity and fractional polarization at λ3.6 cm are presented for eleven radio galaxies, part of a sample of 29 nearby radio galaxies with $P_{178} > 1.5 \times 10^{25}$ W Hz^{-1} sr^{-1}. Ten have classical double structure. The hotspots in all of these are well resolved. We have discovered a one-sided jet in 3C 135, as well as imaging the known jets in 3C 98, 111 and 445 at high resolution. There are also possible jets in five of the remaining six classical doubles. The eleventh object, 3C 15, is well imaged here for the first time. It is dominated by a bright jet and a weak counterjet is also detected.

We point out some of the more common patterns in the structure of the hotspot complexes in our sample, and summarise the frequency with which jets and the various types of hotspot complex are found.

Key words: magnetic fields – polarization – galaxies: active – galaxies: jets – radio continuum: galaxies

1 INTRODUCTION

In an earlier paper (Black et al. 1992: Paper I) we discussed the necessity for detailed imaging of the hotspots in powerful radio sources. These hotspots are a characteristic (but not defining) feature of class II sources in the scheme of Fanaroff & Riley (1974, hereafter FR). They represent the termination of the relativistic beams emanating from the active nuclei of elliptical galaxies; an understanding of the fluid flow processes in them (or even the ability to detect and classify trends and common features) would represent an important advance in our understanding of the physics of the sources as a whole.

To obtain a sample of the nearest bright hotspots, we selected sources from 3CR (Bennett 1962; Spinrad et al. 1985) subject to $z < 0.15$ and $P_{178} > 1.5 \times 10^{25}$ W Hz^{-1} sr^{-1}. (Values of $H_0 = 50$ km s^{-1} Mpc^{-1} and $q_0 = 0$ are assumed throughout, as in Paper I). The power limit is just under the 'FR break', the power below which FR found that most sources have class I structure. These conditions yielded a list of 40 objects, all of which were identified with galaxies rather than quasars. Three of these were too large to observe in the current programme, and 7 were known to be FR I sources or hotspotless 'fat doubles'; these 10 objects were therefore not observed. † Our observations showed that 3C 198 was also a fat double and we have therefore excluded it from the the final sample of 29 sources, which is listed in Table 1. As discussed in Section 5.1, three of these turned out not to be FR II sources in the strict sense, but we retain them as they contain hotspot-like structures.

Ten objects in the final sample were not observed because detailed images had already been made (references are given in Table 1). The remainder were observed with the NRAO Very Large Array (VLA) at λ3.6 cm in B- and C-configurations, and where appropriate in A- and/or D-configurations as well. Images of eight of the sources from the sample were shown in Paper I. The remaining eleven are presented here. For each we show high-resolution images

⋆ Current address: Cambridge University Press, The Edinburgh Building, Shaftesbury Road, Cambridge CB2 2RU

† The description of these omitted galaxies in Paper I was slightly inaccurate. For the record, the FR Is were the wide-angle-tails 3C 89 (Baum et al. 1988) and 3C 130 (Jägers & de Grijp 1985), and the cluster-centre objects 3C 317 and 338 (Ge & Owen 1994); the 'fat doubles' were 3C 310 (van Breugel & Fomalont 1984), 3C 314.1 (Leahy & Perley 1991), and 3C 315 (Leahy & Williams 1984). The three giants were 3C 35 (van Breugel & Jägers 1982), 3C 236 (Barthel et al. 1985) and 3C 326 (Willis & Strom 1978).

of the hotspots together with lower-resolution maps of the whole source.

We restrict discussion in this paper to notes on individual sources, and a brief description of hotspot and jet patterns in the overall sample. In later papers we will present a detailed analysis of the hotspots, and an analysis of the structure of jets and the factors relating to their visibility, with a view to finding which are the most useful in understanding the underlying physics.

2 OBSERVATIONS AND DATA REDUCTION

The observational details are described in Paper I, except that 3C 135 was accidentally omitted from our original C-configuration run and replacement observations were obtained on 1995 Nov 26. Table 2 shows the integration times and bandwidths used for the eleven sources considered here.

The data reduction used the NRAO AIPS software and was carried out as described in Paper I. The *uv* data sets from individual configurations of the telescope were individually time-averaged and self-calibrated and then concatenated with one another to produce a final database. We normally used the 'hybrid' CLEAN/maximum entropy method technique described in Paper I for final mapping in Stokes I and the AIPS task UTESS (based on MEM) for mapping in Stokes Q and U. The majority of the sources imaged here were too large to be mapped adequately in a single pointing; in this case two databases were collected with the observation centres at each end of the source (the preceding and following ends in right ascension are denoted P and F respectively in Table 2). We employed the mosaicing capability of the VTESS family of AIPS tasks to make the low-resolution images of these sources, where this was possible; in some cases primary beam attenuation near the centre of the mosaiced field or problems in deconvolving point sources rendered this impossible, and low-resolution images are presented separately for each lobe. The imaging method adopted for each source is summarized in Table 3.

Table 2. VLA observations for sources presented in this paper

Source	Observation time (minutes)				Bandwidth (MHz)			
	A	B	C	D	A	B	C	D
3C 15	87	—	20	—	50	—	25	—
3C 98P	—	16	19	18	—	25	25	50
3C 98F	—	16	20	19	—	25	25	50
3C 105P	—	36	17	16	—	25	25	50
3C 105F	93	33	19	15	50	25	25	50
3C 111P	—	21	20	8	—	25	25	50
3C 111F	85	19	21	11	50	25	25	50
3C 135	176	49	86	8	12.5	25	50	50
3C 136.1P	—	29	28	11	—	25	25	50
3C 136.1F	—	31	28	8	—	25	25	50
3C 184.1	238	96	21	9	12.5	25	25	50
3C 192	—	71	17	9	—	25	25	50
3C 223P	—	44	19	11	—	25	25	50
3C 223F	—	39	20	11	—	25	25	50
3C 327	240	77	29	16	25	25	25	50
3C 445P	—	30	29	4	—	25	25	50
3C 445F	—	30	28	4	—	25	25	50

Column 1 lists the sources observed with P or F denoting the preceding or following ends of the source, respectively, for those sources which were observed in two pointings. Columns 2–5 list the integration times and 6–9 the bandwidths (in each IF) for each VLA configuration. All observations were at 8235 and 8465 MHz.

3 RESULTS

As in Paper I, the noise levels of the images presented here generally approach the thermal limit; around 40 μJy beam^{-1} in the total intensity images and 28 μJy beam^{-1} in polarized flux. The properties of the final images and data derived from them are summarized in Tables 3 and 4, presented in a format similar to that of Tables 6 and 5 of Paper I.

The jet flux densities listed in Table 4 were determined using a method similar to that of Bridle et al. (1994), with a correction for the background emission from the lobe. Several attempts were made at integration of the jet region itself, including all possible jet components. Similarly shaped regions on either side of the jet region were then integrated, the fluxes were normalised appropriately, and the mean background flux was subtracted from the mean jet region flux to give an estimate of the true jet flux density. The calculated errors in this estimate reflect the differences in the individual measurements but also the variation in background flux on different sides of the jet, which can be the dominant source of error if the jet feature is on the boundary of a region of bright emission (e.g. 3C 223 S1). The region that should be integrated is often not certain, due to confusion with hotspot and lobe structure; these errors are therefore conservative. In appendix A we list similarly corrected jet fluxes for the objects observed in Paper I.

Greyscale images and contour maps are presented. The vectors on the contour maps represent fractional polarization, and their direction is that of the E-vectors; no attempt has been made to correct for the integrated rotation measure of the sources, which is insignificant in most cases (see Table 4). Vectors are drawn only where both the total and polarized intensity signals are above 3σ. Co-ordinates given are J2000.

4 COMMENTS ON INDIVIDUAL SOURCES

In the following notes, we use some terms in a technical sense to avoid ambiguity, and we define them here.

A feature is said to be 'distinct' if it is a brightness peak which

(i) has a largest dimension (FWHM) smaller than 10 per cent of the main axis size of the source;
(ii) has a peak brightness more than ten times the rms noise level;
(iii) is separated from any nearby brighter peaks by a minimum falling to two-thirds or less of the fainter peak.

If there is a single distinct feature in a lobe, we describe it as a hotspot. By a 'hotspot complex' we mean a group of distinct features and surrounding high-brightness

Table 1. The sample of radio galaxies

Name	IAU Name	z	S_{178} Jy	α	$\log(P_{178})$	θ_{LAS} arcsec	D kpc	Ref.
3C 15	0034-014	0.0730	17.2	0.67	25.52	48	92	2
3C 33	0106+130	0.0595	59.3	0.76	25.88	255	404	3,4
3C 98	0356+109	0.0306	51.4	0.78	25.23	310	264	2
3C 105	0404+035	0.089	19.4	0.61	25.74	335	764	2
3C 111	0415+379	0.0485	70.4	0.76	25.77	215	283	2
3C 135	0511+008	0.1273	18.9	0.95	26.07	132	409	2
3C 136.1	0512+248	0.064	15.3	0.72	25.35	460	781	2
3C 184.1	0734+805	0.1182	14.2	0.68	25.87	182	530	2
3C 192	0802+243	0.0598	23.0	0.79	25.47	200	319	2
3C 197.1	0818+472	0.1301	8.8	0.72	25.75	24	76	1
3C 223	0936+361	0.1368	16.0	0.74	26.05	306	1007	2
3C 223.1	0938+399	0.1075	8.1	0.73	25.54	140	376	1
3C 227	0945+076	0.0861	33.1	0.70	25.95	230	510	1
3C 277.3	1251+278	0.0857	9.8	0.58	25.41	49	108	5
3C 285	1319+428	0.0794	12.3	0.95	25.46	180	371	6
3C 303	1441+522	0.141	12.2	0.76	25.96	47	159	7,8
3C 321	1529+242	0.096	14.7	0.60	25.69	307	748	9
3C 327	1559+021	0.1039	38.5	0.64	26.18	302	788	2
3C 353	1717+009	0.0304	257.2	0.74	25.92	284	240	10
3C 382	1833+326	0.0578	21.7	0.59	25.41	185	286	1
3C 388	1842+455	0.0908	26.8	0.70	25.91	50	116	11,12
3C 390.3	1845+797	0.0561	51.8	0.75	25.76	229	345	13
3C 403	1949+023	0.059	28.3	0.74	25.55	230	362	1
3C 405	1957+405	0.0565	9660.0	0.74	28.04	130	197	14
3C 424	2045+068	0.127	15.9	0.88	25.99	35	108	1
3C 430	2117+605	0.0541	36.7	0.75	25.58	90	131	15,16
3C 433	2121+248	0.1016	61.3	0.75	26.37	68	174	1
3C 445	2221-021	0.0562	27.0	0.76	25.48	570	859	2
3C 452	2243+394	0.0811	59.3	0.78	26.15	280	588	1

Sources whose names are in bold type are those for which we present maps in this paper. Redshifts (heliocentric) are from Spinrad et al. (1985). Flux densities at 178 MHz are on the scale of Roger, Bridle & Costain (1973), and were generally determined using the prescription of Laing, Riley & Longair (1983); the following cases are noteworthy. For 3C 223.1 we interpolated from measurements at nearby frequencies, as there is no reliable measurement at 178 MHz. For 3C 403 we use the 3CR value, corrected to the present scale, as there is no 4CT measurement; the value quoted by Kellermann, Pauliny-Toth & Williams (1969), annotated as from 4CT, is actually the 4C value and is clearly affected by partial resolution. For 3C 405 (Cyg A) we use the Baars et al. (1977) value. Spectral indices (generally between 178 and 750 MHz) were also calculated as in Laing et al.. The radio power in column 6 (in W Hz^{-1} sr^{-1}) is calculated from these fluxes and spectral indices. θ_{LAS} is the largest angular size of detected radio emission and D is the equivalent linear size.

References are 1: Paper I; 2: this paper; 3: Rudnick (1988); 4: Rudnick & Anderson (1990); 5: van Breugel et al. (1985); 6: van Breugel & Dey (1993); 7: Kronberg (1986); 8: Leahy & Perley (1991); 9: van Breugel, in preparation; 10: Swain, Bridle & Baum (1996); 11: Burns et al. (1982); 12: Roettiger et al. (1994); 13: Leahy & Perley (1995); 14: Carilli & Harris (1996), and references therein; 15: Spangler, Myers & Pogge (1984); 16: Rudnick, unpublished.

emission (but excluding any features which appear to be part of a jet). We assume there is only one hotspot complex in each lobe; with perhaps one exception, this assumption seems quite unforced. Following Laing (1989), the smallest feature in each complex is called the 'primary hotspot'; note that the primary is often not the brightest feature. The remaining emission constitutes the 'secondary structure'. If the secondary structure is dominated by a single distinct feature we describe that as a 'secondary hotspot'.

The definition of 'distinct' has its drawbacks, but without a formal definition different observers typically disagreed about about the number of features in about a third of cases. The main drawback is that weak features may only be counted on images which happen to have high signal-to-noise; another is that in weak hotspots, random noise may affect whether or not a peak is recognised as distinct. We have tried to avoid the latter problem in highly-resolved hotspots (e.g. 3C 136.1) by checking on images with lower resolution and hence better brightness sensitivity.

Recently Bridle et al. (1994) have also proposed a definition of hotspots. Unlike us they only admit one hotspot per lobe, and their criteria for contrast and compactness are much more restrictive. As a result, several of the luminous FR II quasars that they analysed were considered to lack hotspots in one lobe, and the same would be true for our sample if their definition was used. In a later paper we plan to make a systematic study of various possible operational definitions, with a view to finding the most useful in capturing the underlying physics.

4.1 3C 15

3C 15 has only previously been observed as a low-resolution snapshot by Morganti, Killeen & Tadhunter (1993). The host galaxy is an ordinary elliptical with a close companion and a possible nuclear point source (Fasano, Falomo & Scarpa 1996) and has very weak emission lines (Tadhunter

Table 3. Images for sources presented in this paper

Source	Fig. number	Region	Method	FWHM (arcsec)	FWHM (kpc)	σ_I (μJy)	σ_P (μJy)	Dynamic Range
3C 15	1	Whole	CM	0.34	0.65	19	9	1600
	2	Jet	CM	0.34	0.65	19	9	1600
	3	Whole	C	2.30	4.39	61	39	1600
3C 98	4	Whole	CMm	2.00	1.70	55	27	220
	5	Nf hot spot	CM	0.75	0.64	34	16	135
	6	Sp hot spot	CM	0.75	0.64	25	16	190
3C 105	7	Whole	Cm	2.20	5.02	69	55	5500
	8	Np hot spot	C	1.20	2.74	70	27	24
	9	Sf hot spot	C	0.25	0.57	25	25	2600
3C 111	10	Whole	Cm	2.50	3.28	500	70	2500
	11	Nf hot spot	Cm	1.60	2.10	300	50	910
	12	Nf hot spot	C	0.32	0.42	550	35	59
	13	Sf hot spot	Cm	1.60	2.10	300	50	150
3C 135	14	Whole	C	10.00	31.00	160	–	1000
	15	Whole	CM	2.00	6.20	36	11	1600
	16	Nf hot spot	M	0.30	0.93	26	19	30
	17	Core	C	0.25	0.78	44	16	25
	18	Sp hot spot	M	0.30	0.93	45	25	90
3C 136.1	19	Np lobe	M	2.50	4.25	50	15	80
	20	Np hot spot	M	1.20	2.04	50	18	24
	21	Sf lobe	M	2.50	4.25	53	19	65
	22	Sf hot spot	M	1.20	2.04	42	12	25
3C 184.1	23	Whole	M	2.50	7.28	65	20	510
	24	Np hot spot	C	0.25	0.73	45	15	20
	25	Sf hot spot	C	0.25	0.73	40	14	65
3C 192	26	Whole	C	2.00	3.20	35	20	820
	27	Np hot spot	CM	0.80	1.28	30	10	170
	28	Sf hot spot	CM	0.80	1.28	30	10	170
3C 223	29	Whole	Mm	2.50	8.23	55	25	175
	30	Np hot spot	M	0.75	2.47	37	8	45
	31	Sf hot spot	M	0.75	2.47	40	15	20
3C 327	32	Whole	CM	2.20	5.74	30	30	1300
	33	Np hot spot	C	0.29	0.76	30	30	65
	34	Core	C	0.29	0.76	10	—	2000
	35	Sf hot spot	C	0.29	0.76	13	13	330
3C 445	36	Whole	Cm	2.40	3.62	70	32	1100
	37	Np lobe	CM	2.40	3.62	55	27	660
	38	Np hot spot	CM	1.10	1.66	40	23	410
	39	Sf lobe	CM	2.40	3.62	65	35	530
	40	Sf hot spot	CM	1.10	1.66	57	26	246

Column 3 gives the region covered by each map. Column 4 lists the deconvolution method, where C denotes CLEAN (MX or APCLN), M denotes a maximum entropy algorithm (VTESS or UTESS), and CM is the hybrid method described in Paper I. A lower case m denotes a mosaiced image made using data from two pointings. Columns 5 and 6 give the angular and linear size of the restoring beam. Columns 7 and 8 list the r.m.s. noise on the image (close to the pointing centre) for total and polarized intensity respectively. Column 9 gives the dynamic range, defined as the ratio between the peak intensity and the r.m.s. noise.

et al. 1993). Its radio structure (Fig. 1) appears intermediate between classes I and II of FR, although its luminosity is above that of a number of sources in the sample showing classical FR II structure. These are properties it shares with several small ($\lesssim$ 100 kpc) radio galaxies, for instance 3C 401 (Burns et al. 1984) and apparently with some bright quasars like 3C 9 (Bridle et al. 1994). Law-Green et al. (1995) have christened this class 'jetted double'. 3C 15 has a bright one-sided jet (N1) containing four prominent knots, all resolved (see Fig. 2). The projected magnetic field is initially parallel to the jet, and remains parallel at the jet edges until just before knot D. The on-axis field becomes perpendicular on the downstream side of knot A, and remains more or less perpendicular through the following bright knots; the field then reverts to parallel in the faint ridge in the lobe emission which apparently continues on from the end of the bright jet. The ridge terminates by looping back to the south, without any sign of compact hotspot structure. Much of this structure is remarkably similar to the jet in M 87, although on a scale ten times larger. We emphasise that the jet does not closely resemble those in typical FR Is, which are much smoother.

In the S lobe there is a much weaker counterjet, S1, and a 'warmspot' (S2) at the end of the lobe (it is too large to

Table 4. Properties of sources imaged in this paper

Source	Scale (kpc arcsec^{-1})	Size (kpc)	RM (rad m^{-2})	Jet lobe	Jet feature	Jet flux density (mJy)
3C 15	1.91	92	−12	Np	N1	210 ± 10
				Sf	S1	4 ± 1
3C 98	0.85	264	79	Nf	N1	90 ± 25
3C 105	2.28	764	−65	Sf	S1	50 ± 10
3C 111	1.31	283	−19	Nf	N1	105 ± 10
3C 135	3.10	409	41	Sp	S1	3.1 ± 0.4
3C 136.1	1.70	781	−172	—		
3C 184.1	2.91	530	−14	Np	N1	14 ± 3
3C 192	1.60	319	3	Sf	S1	9 ± 1
3C 223	3.29	1007	14	Np	N1	8 ± 2
				Sf	S1	5 ± 10
3C 327	2.61	788	9	Np	N1	0.43 ± 0.03
3C 445	1.51	859	12	Np	N1	1.3 ± 0.3
				Sf	S1	10 ± 1

Column 4 lists the integrated rotation measures, taken mainly from Simard-Normandin, Kronberg & Button (1981). At 8 GHz, a rotation measure of 100 rad m^{-2} corresponds to a change in polarization position angle of 7 degrees. Column 6 lists the features which have been described as jets in the text, and column 7 gives their flux densities.

count as a hotspot under our definition). The jet-counterjet flux density ratio is 50 ± 10, where the error is due to uncertainty in subtracting the underlying lobe emission from S1. The absence of truly compact features suggests that the jets are dissipative, as is generally believed for FR I radio galaxies (Bicknell 1996). The core and jets are completely surrounded by lobe emission, with no sign of a central gap, and at lower resolution (Fig. 3), the halo shows some faint emission extending along P.A. $-60°$, well off the main axis at P.A. $-30°$; both these facts suggest that the source is well out of the plane of the sky, in which case the jet asymmetry may partially be due to relativistic beaming. Assuming a spectral index of 0.6, typical for jets (Bridle & Perley 1984), the flux asymmetry implies $\beta \cos\theta = 0.635 \pm 0.025$, hence $\theta \approx 45°$–$50°$ for $\beta \gtrsim 0.9$ if all the asymmetry is due to beaming. However, the lack of relatively compact structure resembling S2 in the N lobe suggests that the northern jet is genuinely more dissipative than the southern. Again there is a close similarity with M 87, as interpreted by Biretta, Zhou & Owen (1995).

4.2 3C 98

3C 98 (Fig. 4) was imaged at 5 GHz by Baum et al. (1988), who detected the jet in the N lobe. In our radio images the jet (N1) is seen to be almost continuous between the core and the N hotspot, flaring at the knot N3 (Fig. 5) before entering the compact hotspot N2. The arc-like structure N4 seen leaving the hotspot is most plausibly interpreted in terms of reasonably well-collimated backflow. There is little evidence for a jet in the S lobe, although it may be confused by the internal structure in the lobe; the highly polarized arc S1 is particularly notable. The hotspot S2 is resolved and is extended transverse to the presumed direction of the incoming jet; the grey scale image (Fig. 6) shows its triangular shape.

The host galaxy (Baum et al., Smith & Heckman 1989) is a typical narrow-line radio galaxy (NLRG), with extended narrow emission lines whose kinematics were studied by Baum, Heckman & van Breugel (1990).

4.3 3C 105

A low-resolution 6-cm map is given in Baum et al. (1988). The maps presented here show the same features but in greater detail. The 'hammerhead' structure at the end of the N lobe (Fig. 7) could be interpreted in terms of the recent escape of the lobe from a sharply bounded halo around the host galaxy. If so, the halo would have to extend out to 270 kpc (more, allowing for projection). This is not entirely implausible since 3C 105 is the most isolated of all the radio galaxies studied by Prestage & Peacock (1988). The hotspot N1 is the only compact structure in the lobe, and can be seen in the highest-resolution contour map (Fig. 8) to be extended approximately north-south.

The southern hotspot complex (Fig. 9) dominates the source, to the extent that in the 1.4 and 5 GHz VLA snapshot images by Neff, Roberts & Hutchings (1995) only this region, and its bright tail, were detected, causing them to mis-identify it with the core. (Their maps at 0.35-arcsec resolution show the main features seen in our higher-sensitivity map.) A linear feature, S1, points into an extended peak S2 which merges with the compact component S3. A ridge of emission connects S3 with the bright resolved component S4. There is also complex structure in the fainter emission to the W, including at least two more features which qualify as distinct. The obvious interpretation is to view S1 and perhaps S2 as jet emission, S3 as a jet termination hotspot and S4 as a recent disconnection event as discussed by Cox et al. (1991). The curved overall shape of the complex lends some credibility to this interpretation. In our image S3 is just merged with S2 at the half-power level, and the combined overall size is actually slightly larger than S4, so apparently this interpretation involves the jet entering the secondary rather than the primary hotspot. However the beam-shaped structure of S3 suggests that it is poorly resolved, so that at higher resolution the half-power contour probably would not include S2; thus S3 is probably the true primary. The main problem with this model is that following S1 away from the hotspot complex, it continues to curve and appears to end by pointing into the presumed backflow structure in the lobe rather than into the core. Conceivably, the jet is superposed on a relatively collimated backflow. The wealth of other knots and structure in the complex are in any case suggestive of a rapidly evolving, transient system.

Both the hotspot complexes in 3C 105 are remarkably compact, given the overall size of the source.

The host galaxy is a typical NLRG with only nuclear emission lines (Baum et al. 1988, Smith & Heckman 1989, Tadhunter et al. 1993).

4.4 3C 111

3C 111 is a broad-line radio galaxy with strong X-ray emission (e.g. Nandra & Pounds 1994). An optical image is given by Colina & Pérez-Fournon (1990).

3C 111 has a prominent straight jet (N1) reminiscent of those in higher-power quasars. It has previously been mapped at high resolution by Linfield & Perley (1984; hereafter LP84). The core of the source is very bright (around 1.2 Jy) and variable (its flux increased by 100 mJy between the epochs of our B- and C-configuration observations), and difficulties in correcting for this in multi-epoch, two-pointing observations account for the high level of noise on the total-intensity images. The core appears to be ≈ 1 per cent polarized; this is not simply an instrumental effect, as it is polarized in the same intensity and position angle on maps made from the two different VLA pointings.

The large-scale structure is best seen in the low-resolution image of Leahy & Williams (1984). The hotspots, core, and jet are embedded in a large-scale halo, the brighter parts of which are visible in Fig. 10. The halo is sharply bounded to the SE and W, and the S hotspot complex is sited at the tip of the structure. The main part of the halo is also bounded by a sharp brightness drop to the NE, and the N hotspot and its following tail form a promontory in this border. Very faint emission continues around and well ahead of the N hotspot. A similar case of a hotspot with faint emission ahead of it is found in another broad-lined object, 3C 390.3. It is plausible that the structures of both are significantly distorted by projection, which would also explain why their bridges are continuous across the host galaxies.

The jet is longitudinally polarized (i.e. the B-field is perpendicular) in the few places where polarization can be detected, mainly just as it enters the bright tail behind the hotspot (i.e., before the knot N2, see Fig. 11). Faraday rotation is low in this object, despite its low Galactic latitude (Leahy, Pooley & Riley 1986) and so this unusual orientation can be confirmed on the 1.4 GHz map of LP84. The low-resolution map of Leahy et al. suggests a more normal parallel-field orientation about halfway between core and hotspot. The jet can be traced into the centre of the hotspot tail, but at knot N2 the ridge-line splits (this is also visible on the LP84 maps). Until this point the jet is narrower than the hotspot. It is not clear whether the splitting represents a broadening of the jet to about the width of the hotspot, or whether one of the ridges represents the true jet.

There is no sign of a jet in the southern lobe. The southern hotspot complex is a canonical double, i.e. it has a recessed compact primary (S1) and a more diffuse secondary (S2) at the lobe tip (Fig. 13). Although S1 is only slightly resolved in this tapered image, a 'B'-configuration only image (with about twice the resolution) shows little extra compact structure.

4.5 3C 135

3C 135 is identified with a giant elliptical galaxy in a rich cluster (Smith & Heckman 1989, McCarthy, Spinrad & van Breugel 1995). The galaxy has a fairly compact nucleus, as seen in the HST image (de Koff et al. 1996), but has a narrow-line spectrum (Eracleous & Halpern 1994). McCarthy et al. find slightly extended line emission, suggesting a circumnuclear disk.

The S lobe of 3C 135 has a low-surface-brightness extension to the north, best seen in our D-configuration image (Fig. 14). The intermediate-resolution image (Fig. 15) shows the N lobe to be divided into two unequal segments, separated by a constriction in the lobe boundary, with the smaller outer component of relatively high brightness. A similar structure is found in 3C 349 S (Leahy & Perley 1991). Structures with this sort of scale, ~ 25 per cent of the lobe size, are not uncommon (cf. 3C 15 S, 105 N, 184.1 N). They defy the neat division of lobes into 'bridge' and 'hotspot complex', and suggest instead that discrete structures within the lobe can occur on almost any scale.

We resolve the central component into a double (Fig. 17), of which the eastern component is unresolved and hence represents the true core, while the slightly resolved western component is the first knot in a jet. The faint jet (S1) is detected as it enters the S lobe, but it is not possible to trace it along its length into the bright S hotspot complex. The complex is well recessed from the lobe edges, and its structure is dominated by a bright, sinuous ridge aligned at about 30° to the source axis (Fig. 18). The brightest region of the ridge (S2) is the segment most nearly transverse to the axis. The rest of the complex consists of a diffuse tail to the SE of the ridge, which contains the distinct peak S3.

No jet is detected in the N lobe, but a well-defined double hotspot structure can be seen (Fig. 16). The recessed compact primary, N1, is elongated parallel to the lobe edge, and in the direction of a ridge of highly polarized emission which leads into the more diffuse secondary hotspot, N2. At the southern end of this ridge lies the weak component N3 (which is most distinct on images at resolutions intermediate between those presented here). If the ridge includes N3, then it seems to curve back towards the core at this point, rather than directly linking N1 to N2. The structure is remarkable for the wide separation (in terms of the size of the secondary hotspot) between the components. 3C 33 N has a very similar structure, and feature F3 in 3C 403 may be analogous. In all three cases there is a third feature on the edge of the lobe between the primary and outermost (or 'outlier') component: while very faint in 3C 135, the middle component is brighter than the outliers in the other two.

4.6 3C 136.1

3C 136.1 is a large source with 'wings' which are visible at low frequency and resolution (Leahy & Williams 1984). The host galaxy has not been studied in detail because it is at low Galactic latitude: in particular, it is not known whether it is a broad- or narrow-line radio galaxy, although it is known to have strong emission lines. The radio images presented here are not sensitive enough to show the lobes near the core (due to primary beam attenuation and limited short-baseline *uv* coverage), and we have not attempted to make a single image covering the whole source: Fig. 19 shows the shorter Np lobe (and the core), and Fig. 21 the Sf lobe, at intermediate resolution. The hotspots (Figs 20 & 22) show unusually little compact structure; the brightest points (N1 and N2 in the northern lobe, S1 in the southern) have little contrast with their surroundings. Because of the low contrast of the internal structure, we classify the N hotspot as a single component. There is a faint compact feature S2 to the NW of, and barely distinct from, S1. As the most compact feature in the lobe, S2 qualifies as the primary hotspot.

There is no indication of a jet in these images.

4.7 3C 184.1

The large-scale radio structure of 3C 184.1 was imaged by Miller (1985) and Leahy & Perley (1991), and Miller (1983) presented VLA 5-GHz images of the hotspots. The host is an elliptical NLRG, recently imaged with HST by de Koff et al. (1996).

Our maps show details of the hotspots projecting from the lobes. In the N lobe (Fig. 24), a curving jet-like feature (N1) at low surface brightness seems to run into the hotspot complex through the region of bright diffuse emission to its SE; the hotspot complex itself (N2) is resolved and extends E-W transverse to the presumed jet direction. If N1 is a jet, the underlying beam is remarkable for undergoing two ninety-degree bends (one visible in the map in Fig. 24, one inferred if it is to point towards the core). An alternative hypothesis is that it represents collimated outflow from the hotspot. The low-contrast structure within N2 appears to break it up into about three distinct components, but this is uncertain due to the low signal-to-noise ratio.

The S lobe has no evidence for a jet; the hotspot (Fig. 25) is extended E-W and its boundary is a smooth curve.

4.8 3C 192

3C 192 is also imaged in Miller (1985). The source is well known for its X-symmetry, which is best seen in the 1.5 GHz map of Laing & Spangler, published by Baum et al. (1988). Unlike the extreme cases of 'wings' seen in 3C 136.1, 223.1 and 403, this kind of structure can be explained by backflow (cf. Leahy & Williams 1984, Miller 1985). The host NLRG shows extended line emission, whose kinematics have been studied by Baum et al. (1990).

The images of the N hotspot (Fig. 27) show a pair of very faint filaments, polarized transverse to their length (N4 and N5) which appear to lead into the hotspot. It is not clear whether either of these can be identified as a jet; they may be more closely related to the 'spur' near hotspot A of Cyg A (Carilli et al. 1991), which appears to be an outflow from the hotspot. The hotspot itself (N1) is compact but surrounded by bright resolved structure, a high-intensity region (N2) extending predominantly to the south, and a fainter, slightly edge brightened component (N3) to the north (note that the central contour in N3 surrounds a minimum).

The ring-like S hotspot complex is connected to the lobe by a highly polarized 'neck' (Fig. 26). Its detailed structure (Fig. 28) admits two classes of interpretation. In one, suggested by the ring in the western lobe of 3C 353, the ring is a structure (perhaps a vortex tube) surrounding the end of a very decollimated jet. The other, which we prefer, sees the ridge S1 as part of a jet, with the flow continuing, with some decollimation, around the boundary of the hotspot complex through S2 to S3, and perhaps on to the faint component S4. The polarization (with the magnetic field everywhere aligned along the ring) is consistent with either of these interpretations. The 'jet' flux density depends critically on which of these components are considered to be jet knots and which hotspots. We applied the criteria of Bridle et al. (1994), which marginally favour S2 as the end of the jet (and hence the primary hotspot), on the basis of decollimation and a fairly substantial change of direction; thus the jet flux we list in Table 4 includes the emission up to but not including S2. The element of ambiguity in this choice reflects the fact that the difference between jet and hotspot, though often clear, is at root a matter of convention.

4.9 3C 223

The host NLRG dominates a group of about 12 galaxies, and may have slightly extended emission lines (Baum et al. 1988, Smith & Heckman 1989); de Koff et al. give an HST image. The group is much smaller than the giant radio source, whose large-scale structure is best seen in the image by Leahy & Perley (1991). Our dataset undersamples the largest angular scales, and so some diffuse emission is missing from the maps presented here.

Our low-resolution map of the whole source (Fig. 29) shows a faint linear feature in each lobe (denoted N1 and S1) which might conceivably be jets. The one in the S lobe does not point directly into the hotspot complex, however, and is confused by the filamentary structure seen in the rest of the lobe. At high resolution (Fig. 30) the triangular N hotspot is seen to contain two bright extended peaks N2 and N3 on either side of the source axis (but the minimum between them is not quite enough for them to qualify as distinct components). N3 is the brighter and more compact peak, but the jet-like feature N1 appears to point into N2. Both features are polarized transverse to their length.

The S hotspot complex is resolved at the higher resolution (Fig. 31) into two components S2 and S3, with the latter being extended roughly E-W.

4.10 3C 327

The host galaxy is an NLRG (Simpson et al. 1996) with a slightly extended nuclear emission region (Baum et al. 1988). Optical images are given by Baum et al. and Smith & Heckman (1989). The radio structure was observed at lower resolution by Baum et al.. The low-resolution map presented here (Fig. 32) shows the same features.

At the highest resolution there are features around the core at the 5σ level in the position angle required for a possible jet and counterjet (Fig. 34). There are indications of long, extremely low-contrast jets in both lobes, but confusion with other lobe structures (and thermal noise) make it impossible to confirm their reality.

The brightest peak of the northern hotspot (Fig. 33) is N3, extended roughly N-S. It is not clear whether the extended feature N2 forms part of a jet.

The southern lobe contains a canonical double hotspot with an elongated primary S1 which appears to be 'feeding' a more diffuse secondary hotspot S2 which contains several low-contrast peaks (Fig. 35). Both components are contained in a high-brightness region with a roughly parabolic outer edge, with S1 projected on the edge.

A relatively bright tail extends behind S1 and S2 (see Fig. 32; note that the components visible in Fig. 35 correspond to the burnt-out region in Fig. 32). The internal structure of the tail includes three low-contrast peaks (S3, S4, and S5) which just qualify as distinct. Such 'tail' emission is also included by our definition in the hotspot complexes of 3C 223.1 N (N3) and S (S4), 3C 227 P (component P4), and 3C 445 S (S3). It does not seem very natural to call such features hotspots, but they would certainly be so called if the brighter components (e.g. S1&2 in 3C 327) were not present, so we go along with our formal definition.

The whole region containing S1–S5 is embedded in a lower-brightness lobe, which has its own parabolic boundary on a larger scale (Fig. 32).

4.11 3C 445

Optical images of this broad-line radio galaxy are given by Smith & Heckman (1989) and Colina & Pérez-Fournon (1990). Eracleous & Halpern (1994) have studied the broad-line profiles.

In the radio it was previously observed by Kronberg, Wielebinski and Graham (1986) with the VLA at 1.4 and 5 GHz. Their 1.4 GHz map shows evidence for broadening of the source towards its centre which is not seen in our maps (which suffer from primary beam attenuation and undersampling). The jet S1 seen on their map is more clearly defined in our images (Figs. 36, 39), and seems to be a suddenly terminating 'partial jet' like that of 3C 219 (Clarke et al. 1992). As in 3C 219, there is also a 'counter-jet knot', N1 (Fig. 36).

The north end of the source (Fig. 37) can be considered as a very large double hotspot, of which the more diffuse secondary hotspot (N3) is essentially resolved out in our full resolution image (Fig. 38), which just shows the compact primary N2. There is also a smaller and fainter third component N4 between N2 and N3.

The south end (Fig. 39) shows a bright hotspot (S2: Fig. 40) extended E-W along the extreme edge of the source. A more diffuse secondary feature (S3) lies just behind.

5 DISCUSSION

5.1 Overall structure

Of the 29 objects in our sample, 26 are FR IIs in the original sense; that is, the separation between the peaks in the two lobes is greater than half the largest angular size. The remaining three (3C 15, 424 and 433) do not obviously fit into existing classifications: all are formally FR I on the basis of the images presented here, although they all contain hotspot-like compact features in their lobes and have luminosities well above the FR break. As noted above, 3C 15 is a typical jetted double, with one lobe basically FR I while the other is basically FR II. 3C 424 could be interpreted as a highly collimated FR II (with hotspots at S2 and N1) expanding into a relaxed older structure. 3C 433 could also be shoehorned into the jetted double category, as a very distorted example. It becomes an FR II in images with slightly lower resolution than that in Paper I, because the extended peak S4/S5 at the tip of the S lobe becomes more prominent. However, the attempt to classify it is probably rather irrelevant given that the structure is quite unlike any other known radio source, and the gas-rich host galaxy is also extremely unusual (van Breugel et al. 1983, de Koff et al. 1996).

Of the FR II objects, most are conventional classical doubles in the sense that they contain hotspot complexes at or near the end of each lobe. Exceptions are 3C 277.3, with a hotspot only in the north lobe (it is another jetted double); and 3C 388, which like 3C 424 has diffuse outer lobes (but this time much closer to the scale of the inner classical double). Thus, ignoring 3C 433 and excluding the hotspotless lobes of 3C 15 and 277.3, we have 54 'classical' lobes in the sample.

There is no obvious relationship between total source luminosity and overall source structure; both unusual objects and normal classical doubles are distributed throughout the luminosity range of the sample. This is exemplified by 3C 98, the least luminous object, which is as close to an archetypical classical double as one could wish, and by 3C 433, the second most luminous, whose structure is highly distorted.

5.2 Hotspots

Our analysis of the systematics of hotspot structure is based on that of Black (1992, 1993), although our terminology has been significantly revised and redefined, in part to take into account the concept of hotspot complexes.

The locations within the lobes of the hotspot complexes are given in column 2 of Table 5. Here 'side' is anywhere on the lobe boundary except the extreme tip; 'internal tip' and 'internal side' refer to the tip or side of a distinct structure internal to the lobe; 'middle' just means not on any such surface. Most hotspot complexes (36 out of 54) are at the lobe tip. Of the 18 which are set back somewhat, 5 are on the lobe boundary while 7 are set on the boundary of a well-defined bright region within the lobe. As discussed for 3C 111 above, some of these 'internal boundaries' may represent the actual lobe surface seen projected through other parts of the structure. In other cases, as for instance in the south lobe of 3C 327, the fainter outer sheath of the lobe may represent a shear layer in which the pressure is partially maintained by a thermal component (cf. Leahy & Perley 1991). The

Table 5. Hotspot structure of FR II lobes

Lobe	Location	Type	Comments
3C 15 S	side	0	jet; warmspot
3C 33 N	tip	2+1	recessed primary; flaring?; outlier; rim?
3C 33 S	tip	2	symmetric tip; primary at tip; rim
3C 98 N	tip	1	jet enters hotspot
3C 98 S	middle	1	
3C 105 N	tip	1	
3C 105 S	tip	2+2	rim; jet? enters primary?
3C 111 N	internal tip	1	jet nears hotspot
3C 111 S	tip	2	recessed primary
3C 135 N	tip	3	recessed primary; rim; outlier
3C 135 S	middle	2	jet
3C 136.1 N	tip	1	
3C 136.1 S	tip	2?	recessed primary?
3C 184.1 N	tip	M?	rim? jet? nears hotspot
3C 184.1 S	tip	1	rim; flaring?
3C 192 N	tip	1	jet?
3C 192 S	tip	M	rim; ring; jet?
3C 197.1 N	tip	2?	Poorly resolved
3C 197.1 S	internal side	1	rim?
3C 223 N	tip	1	jet? flaring?
3C 223 S	tip	2	rim? jet?
3C 223.1 N	tip	2	rim; jet?
3C 223.1 S	tip	3+1	symmetric tip; rim
3C 227 P	tip	3	2 equal size
3C 227 F	tip	2	primary in centre
3C 277.3 N	tip	1	
3C 285 P	side	1	ring; jet?
3C 285 F	side	1	jet nears hotspot
3C 303 P	middle	3?	jet enters primary
3C 303 F	tip	1	unresolved
3C 321 N	tip	2	poorly-resolved rim; jet
3C 321 S	internal side	1	jet nears hotspot
3C 327 N	side; internal tip	1	rim; flaring? jet?
3C 327 S	internal tip	2+3	recessed primary; rim? jet?
3C 353 P	side	2	ring; jet
3C 353 F	middle	1?	jet enters hotspot; flaring
3C 382 N	tip	1	jet enters hotspot
3C 382 S	tip	2	secondary ring
3C 388 P	middle	1	jet enters hotspot; flaring
3C 388 F	middle	1	jet
3C 390.3 N	tip	M	jet enters recessed primary
3C 390.3 S	internal tip	3+1	rim; jet nears hotspot; jet? enters primary
3C 403 P	tip	1	peak on side; rim?
3C 403 F	tip	3+4?	outlier; rim; jet enters primary (twice?)
3C 405 P	tip	2+?	recessed primary; jet near hotspot
3C 405 F	tip	2+?	jet enters recessed primary
3C 424 N	internal tip	1	unresolved
3C 424 S	internal tip	1	poorly resolved; jet nears hotspot
3C 430 N	tip	1+1	rim primary at tip
3C 430 S	tip	2	equal size; rim
3C 445 N	tip	1+2	primary at tip; outlier? rim? jet?
3C 445 S	tip	1+1	rim primary at tip; jet
3C 452 P	tip	2	recessed primary; jet
3C 452 F	tip	2	primary on rim; jet

'?' signifies uncertain classification or detection.

6 complexes not located on obvious surfaces are about the minimum we would expect from projection effects alone.

As noted in Paper I, some structure, in the sense of sharp edges, is still unresolved in our images. On the other hand all but the physically smallest objects (3C 197.1, 303 and 424) are well resolved in the sense that the FWHM of the most compact peak is greater than about twice the smallest beamwidth with which they have been observed.‡ Precise definition of hotspot sizes is a knotty problem which we defer to a later paper, because many hotspot complexes contain structure on several scales. However FWHM sizes of the smallest bright peaks range from about 1 to 30 kpc. On the whole these seem to be somewhat larger than the sizes <1–4 kpc quoted by Laing (1989) in his definition of the primary hotspots found in much more luminous FR IIs. Almost inevitably, the largest components are found in the largest objects (for instance, 3C 445 N3 is comparable in size to an entire lobe in 3C 197.1; a feature like this could only be described as a hotspot when part of a very large source). More significantly, the smallest components tend to occur in the smallest objects (e.g. the hotspots in 3C 197.1 and 3C 424). However, there is a huge scatter in any scaling relationship. We do not believe that these results are biased by the factor of five range in redshift within the sample, because this is largely compensated for by our choice of the largest VLA configuration to use in each case; our highest linear resolution was 0.4 kpc in 3C 111, while even for the most distant objects we could get a resolution of 0.8 kpc when necessary.

In Paper I we emphasised the diversity of hotspot structures. The present results also include a number of unique structures (e.g. 3C 15 S, 3C 135 S), but some patterns are beginning to emerge. Column 3 of Table 5 classifies the hotspot complexes of all 54 lobes in terms of the number of distinct features within the complex; 'M' (for many) indicates particularly complicated structure. When there are extremely faint features (with peak brightnesses less than 10 per cent of the complex maximum) use the notation X+Y, where X is the number of bright features and Y is the number of faint ones.

Laing (1989) described two 'characteristic' hotspot structures (which are not meant to be exhaustive): 'double' and 'flaring'. Both featured a compact primary, and differ according to whether the secondary structure consists of a discrete secondary hotspot or of a 'curved emitting region expanding away' from the primary.

Unlike Laing, we frequently find three or more distinct features within a hotspot complex. In most of these cases, one or two features are significantly brighter than the rest, and we may simply be recognising fainter components than Laing would have considered (but there are at least three discrete bright hotspots in 3C 403 F). We have thirty-one hotspot complexes containing multiple distinct features. Although all contain a primary hotspot by definition (i.e., the smallest feature), only in about fifteen of them is the primary less than half the size of any other component, and there are three clear cases where the two brightest components are both compact, with FWHM sizes differing by 50 per cent or less (227 P, 405 F and 430 S). Most of the primaries are clearly recessed relative to the secondary structure, as found by Laing. In the few cases where the primary is at the tip (as in 3C 33 N and both ends of 3C 445), the secondary structure is much fainter than the primary. Laing identified the primary as the jet termination point. Consistent with this we have four clear examples where a jet enters a primary (noted in Table 5) and none where one enters a secondary; however three of the clear examples were already known to Laing. The fourth example, 3C 403 F, arguably contains two primaries, F6 and F1, each at the end of a jet segment (this is the one lobe which might be said to contain two hotspot complexes). There are also two cases where possible jets enter a multiple hotspot: in 3C 390.3 S the putative jet enters the primary, but 3C 105 S is more ambiguous, as discussed earlier. In any case, the existence of some similarly-sized pairs of hotspots shows that 'secondary' structures (whichever they are) can be compact, and raises the possibility that Laing's size criterion may not always correctly identify the end of the jet.

Unlike double (or multiple) hotspots, Laing's 'flaring' type appears to be rare in our sample. In this paper, 3C 223 N provides the closest fit (not wholly convincingly), and there are only two clear examples altogether (3C 353 F and 388 P). Unfortunately, Laing gives only a single type example so it is not clear whether we are using the term in quite the same sense; furthermore Laing gives no data on the frequency with which the types occur, so it is not possible to say if our sample is really different in this respect from Laing's more luminous objects.

Another common structure, noted already by Dreher (1981), is a bright rim. This may define the edge of the large-scale lobes (e.g. 3C 135 N), but more often bounds intermediate-scale structure in the hotspot complex (e.g. 3C 390.3 S). The two cases just cited have quite complete rims, but we also include here shorter segments as in 3C 445 S. At least 15 and perhaps up to 22 hotspots can be described in this way. This category overlaps with both multiple and flaring hotspots; for instance multiple features can often be considered as prominent peaks on a rim.

The most extreme of the rim hotspots is the nearly complete ring in 3C 192 S. This might be better grouped with the ring hotspots found in 3C 285 P and 353 P, which do not mark the boundaries of lobes. Such ring structures merge into large-scale ring features, as in 3C 382 P (which we describe tentatively as a secondary hotspot) or 3C 303 F (which takes up most of the lobe).

Finally we note that among the diversity, remarkably similar structures do occur, such as the very symmetrical complexes 3C 33 S and 223.1 S, and the 'outlier' hotspots widely separated from the primary in 3C 33 N, 135 S, and 403 F.

5.3 Jets

In table 5 we note all the lobes containing jets or possible jets (denoted 'jet?'). All the definite jets meet the the operational definition of Bridle & Perley (1984). Possible jets are generally discussed in the notes on individual sources. We adduce a possible jet in 3C 285 P based on a very faint but apparently compact elongated knot between the core and

‡ In 3C 430, the peaks are unresolved on the 1.8-arcsec resolution image of Spangler et al. (1984), but are clearly resolved in the 0.5-arcsec resolution images of Rudnick (unpublished).

the lobe, which peaks at two contours in the image of van Breugel & Dey (1993).

All three of the 'problem sources' discussed in section 5.1 show jets. Of the 26 FR IIs, 15 (58 per cent) now have clearly detected jets, including 6 (23 per cent) with definite jets in both lobes. Including the jetted lobe of 3C 15, 22 (41 per cent) of our 54 lobes with hotspots contain definite jets. Since we had hoped that these observations would help clarify the jet-hotspot interaction, it is disappointing that only in 14 cases do the jets even approach the hotspots, and only in 8 cases is the detailed connection fairly unambiguous: these are noted in Table 5.

As discussed by Black (1992, 1993), our jet detection rate is much higher than in previous samples of FR II radio galaxies, almost certainly because of our high resolution and sensitivity rather than because we have selected relatively low-luminosity examples. Even now, the five objects lacking any sign of jets have images of distinctly below average quality.

6 CONCLUSIONS

We have presented new images of eleven radio galaxies, completing publication of the data for this project.

The hotspots show a variety of detailed structures, but in our total sample, a few broad patterns can be discerned, including rim-brightened hotspots as described by Dreher (1981), double hotspots more-or-less as described by Laing (1989), and more rarely, ring structures.

We have found jets for the first time in two objects, and imaged known jets in three more. Two objects have twin jets (3C 15 and 445). There are also possible jets in five more objects. Jets are now detected in well over half of our sample, thanks to the high quality of the images.

ACKNOWLEDGEMENTS

We are very grateful to Wil van Breugel and Larry Rudnick for allowing us access to their images of 3C 285, 3C 321, and 3C 430 in advance of publication. ARSB, MJH and JD-T thank SERC and its successor PPARC for research studentships. SSK thanks the Royal Society and the University of Manchester for financial support during work on this project. The National Radio Astronomy Observatory is operated by Associated Universities Inc, under cooperative agreement with the National Science Foundation. This project made use of STARLINK facilities. This research has made use of the NASA/IPAC Extragalactic Database (NED) which is operated by the Jet Propulsion Laboratory, California Institute of Technology, under contract with the National Aeronautics and Space Administration.

REFERENCES

Baars J. W. M., Genzel R., Pauliny-Toth I. I. K., Witzel A., 1977, A&A, 61, 99
Barthel P. D., Schilizzi R. T., Miley G. K., Jägers W. J., Strom R. G., 1985, A&A, 148, 243
Baum S. A., Heckman T., Bridle A., van Breugel W., Miley G., 1988, ApJS, 68, 643
Baum S. A., Heckman T., van Breugel W., 1990, ApJS, 74, 389
Bennett A., 1962, Mem. RAS, 68, 163
Bicknell G. V., 1996, in Hardee P. E., Bridle A. H., Zensus J. A., eds, ASP Conf. Ser. 100, Energy Transport in Radio Galaxies and Quasars. Astron. Soc. Pac., San Francisco, p. 253
Biretta J. A., Zhou F., Owen F. N., 1995, ApJ, 447, 582
Black A. R. S., 1992, PhD thesis, University of Cambridge
Black A. R. S., 1993, in Röser H.-J., Meisenheimer K., eds, Jets in Extragalactic Radio Sources. Springer-Verlag, Berlin, p. 15
Black A. R. S., Baum S. A., Leahy J. P., Perley R. A., Riley J. M., Scheuer P. A. G., 1992, MNRAS, 256, 186 (Paper I)
Bridle A. H., Hough D. H., Lonsdale C. J., Burns J. O., Laing R. A., 1994, AJ, 108, 766
Bridle A. H., Perley R. A., 1984, ARAA, 22, 319
Burns J. O., Christiansen W. A., Hough D. H., 1982, ApJ, 257, 538
Burns J. O., Basart J. P., De Young D. S., Ghiglia D. C., 1984, ApJ, 283, 515
Carilli C. L., Harris D. E., eds, 1996, Cygnus A — Study of a Radio Galaxy. Cambridge University Press, Cambridge
Carilli C. L., Perley R. A., Dreher J. W., Leahy J. P., 1991, ApJ, 383, 554
Clarke D. A., Bridle A. H., Burns J. O., Perley R. A., Norman M. L., 1992, ApJ, 385, 173
Colina L., Pérez-Fournon I., 1990, ApJS, 72, 41
Cox C. I., Gull S. F., Scheuer P. A. G., 1991, MNRAS, 252, 558
de Koff S., Baum S. A., Sparks W. B., Biretta J., Golombek D., Machetto F., McCarthy P., Miley G. K., 1996, ApJS, 107, 621
Dreher J. W., 1981, AJ, 86, 833
Eracleous M., Halpern J. P., 1994, ApJS, 90, 1
Fanaroff B. L., Riley J. M., 1974, MNRAS, 167, 31P (FR)
Fasano G., Falomo R., Scarpa R., 1996, MNRAS, 282, 40
Ge J., Owen F. N., 1994, AJ, 108, 1523
Jägers W. J., de Grijp M. H. K., 1985, A&A, 143, 176
Kellermann K. I., Pauliny-Toth I. I. K., Williams P. J. S., 1969, ApJ, 157, 1
Kronberg P. P., 1986, Can. J. Phys., 64, 449
Kronberg P. P., Wielebinski R., Graham D. A., 1986, A&A, 169, 63
Laing R., 1989, in Meisenheimer K., Röser H.-J., eds, Hot Spots in Extragalactic Radio Sources. Springer, Berlin, p. 27
Laing R. A., Riley J. M., Longair M. S., 1983, MNRAS, 204, 151
Law-Green J. D. B., Leahy J. P., Alexander P., Allington-Smith J. R., van Breugel W. J. M., Eales S. A., Rawlings S. G., Spinrad H., 1995, MNRAS, 274, 939
Leahy J. P., Perley R. A., 1991, AJ, 102, 537
Leahy J. P., Perley R. A., 1995, MNRAS, 127, 1097
Leahy J. P., Pooley G. G., Riley J. M., 1986, MNRAS, 222, 753
Leahy J. P., Williams A. G., 1984, MNRAS, 210, 929
Linfield R., Perley R., 1984, ApJ, 279, 60 (LP84)
McCarthy P. J., Spinrad H., van Breugel W., 1995, ApJS, 99, 27
Miller L., 1983, PhD thesis, University of Cambridge
Miller L., 1985, MNRAS, 215, 773
Morganti R., Killeen N. E. B., Tadhunter C. N., 1993, MNRAS, 263, 1023
Nandra K., Pounds K. A., 1994, MNRAS, 268, 405
Neff S. G., Roberts L., Hutchings J. B., 1995, ApJS, 99, 349
Prestage R. M., Peacock J. A., 1988, MNRAS, 230, 131
Roettiger K., Burns J. O., Clarke D. A., Christiansen W. A., 1994, ApJ, 421, L23
Roger R. S., Bridle A. H., Costain C. H., 1973, Astr. J., 78, 1030
Rudnick L., 1988, ApJ, 325, 189
Rudnick L., Anderson M., 1990, ApJ, 355, 427
Simard-Normandin M., Kronberg P. P., Button S., 1981, ApJS, 45, 97
Simpson C., Ward M., Clements D.L., Rawlings S., 1996, MNRAS, 281, 509
Smith E. P., Heckman T. M., 1989, ApJS, 69, 365

Table A1. Corrected jet flux densities for the sources in Paper I

Source	Jet lobe	Jet feature	Jet flux density (mJy)
3C 197.1	–		
3C 223.1	Np	N4	2.5 ± 0.5
3C 227	–		
3C 382	Np	N2,4,5,6	31 ± 2
3C 403	Nf	F4,5,6,7,8	80 ± 10
3C 403[a]	Nf	F7,8	7.8 ± 0.6
3C 424[b]	Np	N1,2,3	38 ± 3
	Sf	S1,2	48 ± 1
3C 433	Np	N1,2,3,4	47 ± 9
3C 452	Nf	F4,5	16 ± 3
	Sp	P4,5	30 ± 7

[a] We quote two values for 3C 403, which assume that the jet ends at F1 and F6 respectively.
[b] In section 5.1 we discuss a model for 3C 424 in which only S3 is a possible component of a jet. If this model is correct, the background-corrected jet flux of the Sf component of 3C424 is 15 ± 1 mJy, and there is no Nf jet feature.

Spangler S. R., Myers S. T., Pogge J. J., 1984, AJ, 89, 1478
Spinrad H., Djorgovski S., Marr J., Aguilar L., 1985, PASP, 97, 932
Swain M. R., Bridle A. H., Baum S. A., 1996, in Hardee P. E., Bridle A. H., Zensus J. A., eds, ASP Conf. Ser. 100, Energy Transport in Radio Galaxies and Quasars. Astron. Soc. Pac., San Francisco, p. 299
Tadhunter C. N., Morganti R., di Serego Alighieri S., Fosbury R. A. E., 1993, MNRAS, 263, 999
van Breugel W., Balick B., Heckman T., Miley G., Helfand D., 1983, AJ, 88, 40
van Breugel W. J. M., Dey A., 1993, ApJ, 414, 563
van Breugel W., Fomalont E. B., 1984, ApJ, 282, L55
van Breugel W., Jägers W., 1982, A&AS, 49, 529
van Breugel W., Miley G., Heckman T., Butcher H., Bridle A., 1985, ApJ., 290, 496
Willis A. G., Strom R. G., 1978, A&A, 62, 375

APPENDIX A: MEASUREMENT OF JET FLUX DENSITIES

In Table 5 of Paper I, flux densities for features classed as possible jets were given without correction for the background flux of the lobe. In Table 4 of this paper we present background-corrected jet fluxes; for completeness, we list here (Table A1) the equivalent fluxes for the objects presented in Paper I. The correction for background flux is described in Section 3.

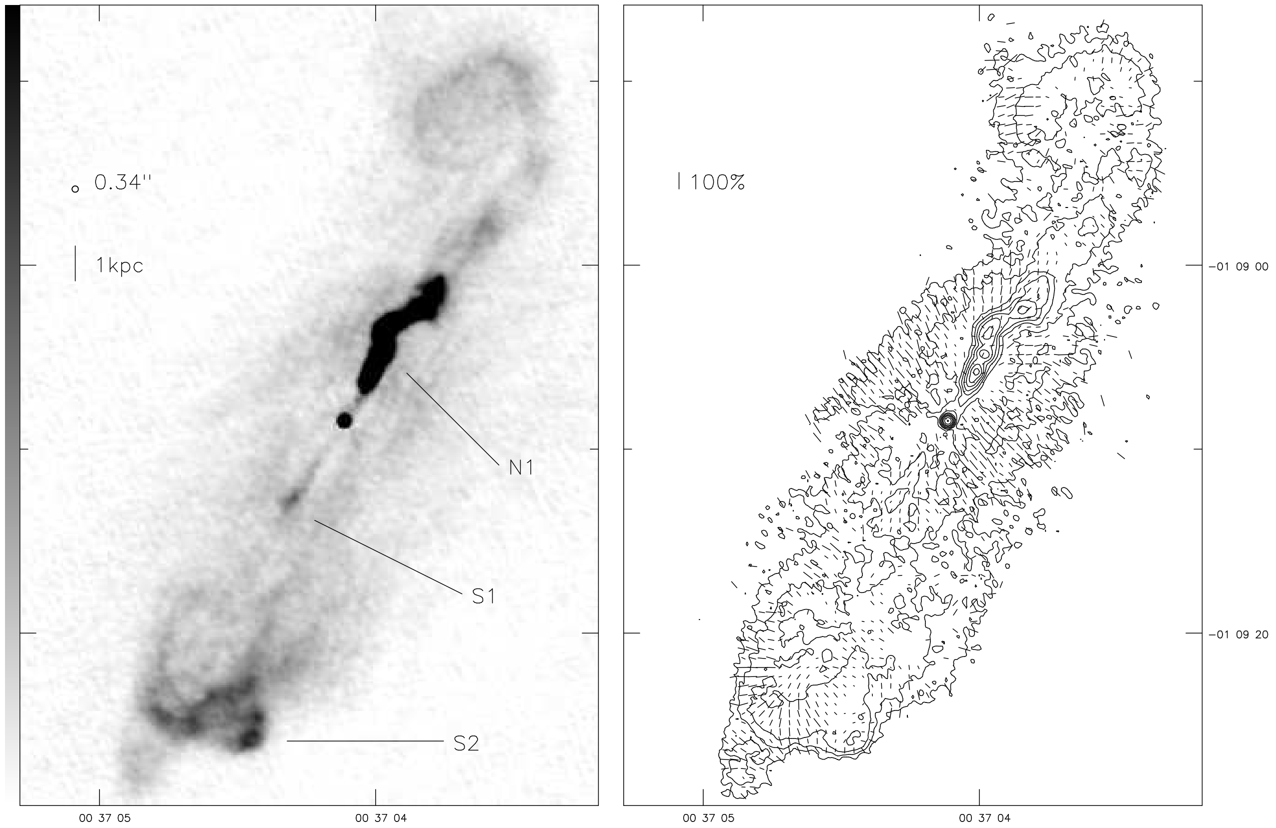

Figure 1. 3C15 at 0.34 arcsec resolution. (a) Linear greyscale; black is 1 mJy beam^{-1}. (b) Contours at $0.1 \times (-2, -1, 1, 2, 4, \ldots)$ mJy beam^{-1}. Negative contours are dashed.

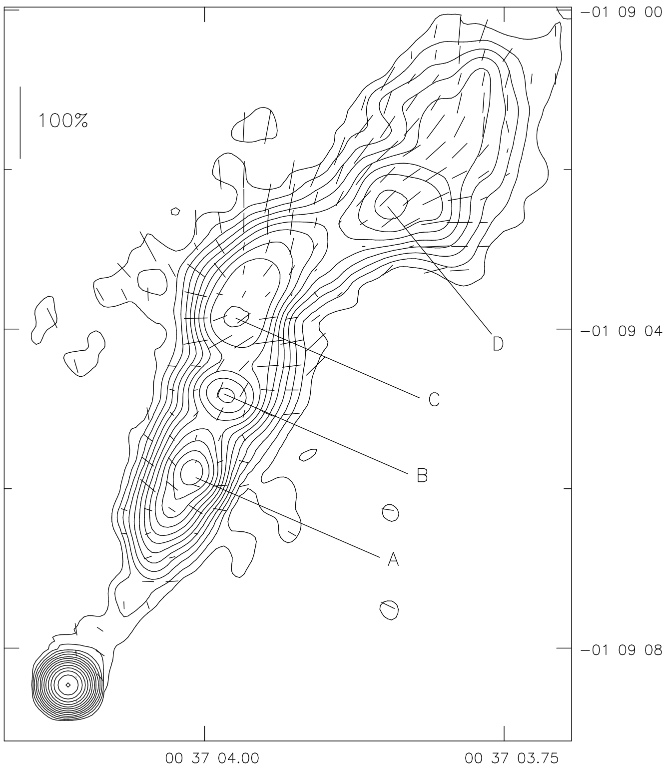

Figure 2. Jet of 3C15 at 0.34 arcsec resolution. Contours at $0.3 \times (-\sqrt{2}, -1, 1, \sqrt{2}, 2, 2\sqrt{2}, \ldots)$ mJy beam^{-1}. Negative contours are dashed. Polarization clipped at lowest positive contour level for ease of presentation.

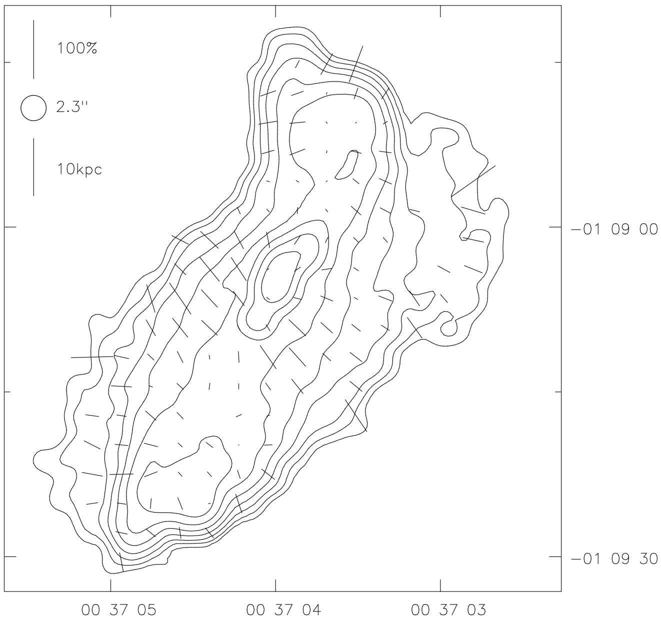

Figure 3. 3C15 at 2.30 arcsec resolution. Contours at $0.2 \times (-2, -1, 1, 2, 4, \ldots)$ mJy beam^{-1}. Negative contours are dashed.

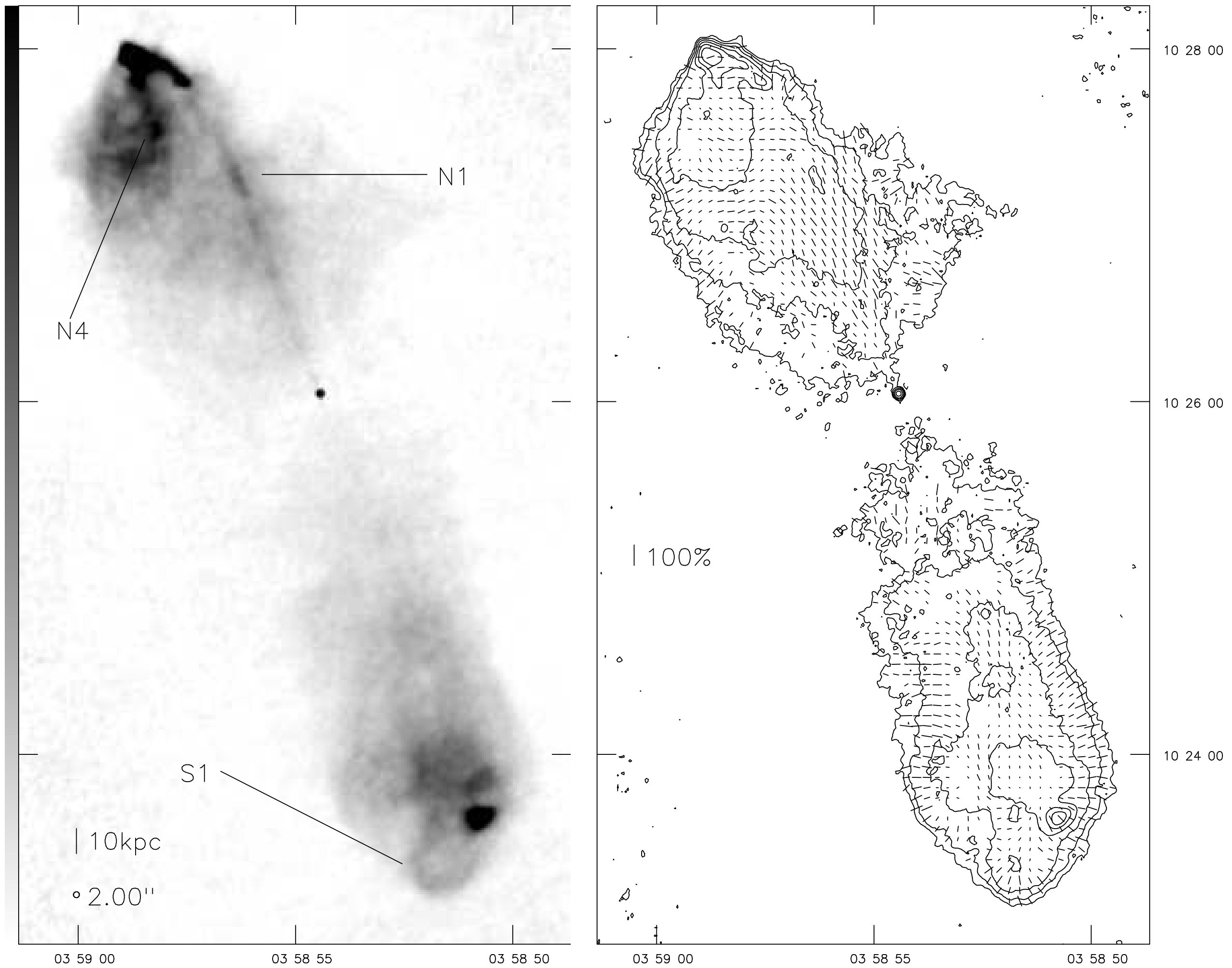

Figure 4. 3C98 at 2.0 arcsec resolution. (a) Linear greyscale; black is 3 mJy beam^{-1}. (b) Contours at $0.2 \times (-2, -1, 1, 2, 4, \ldots)$ mJy beam^{-1}. Negative contours are dashed.

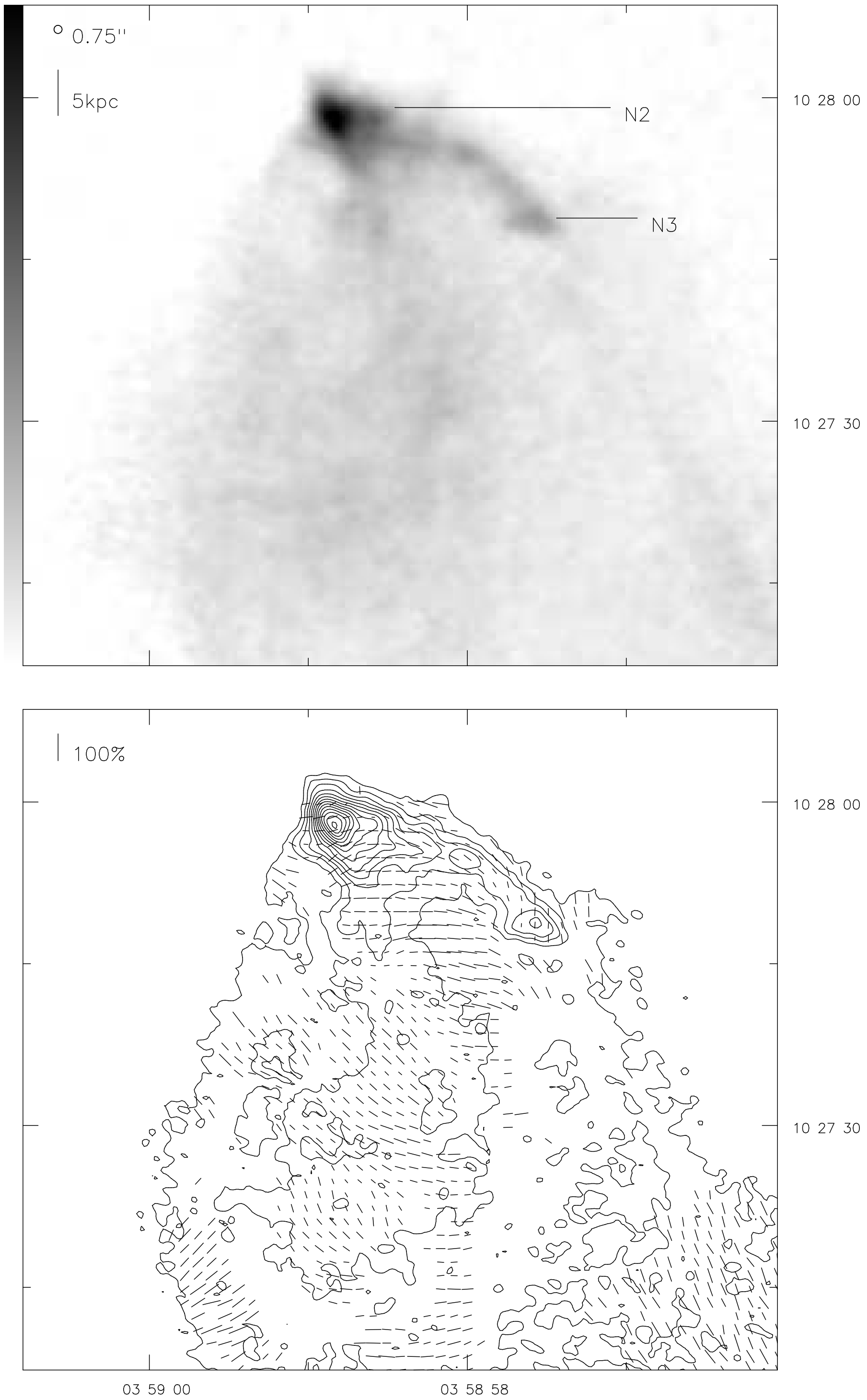

Figure 5. Nf hotspot of 3C98 at 0.75 arcsec resolution. (a) Linear greyscale; black is 2 mJy beam^{-1}. (b) Linear contours at $0.15 \times (-2, -1, 1, 2, 3, 4, \ldots)$ mJy beam^{-1}. Negative contours are dashed.

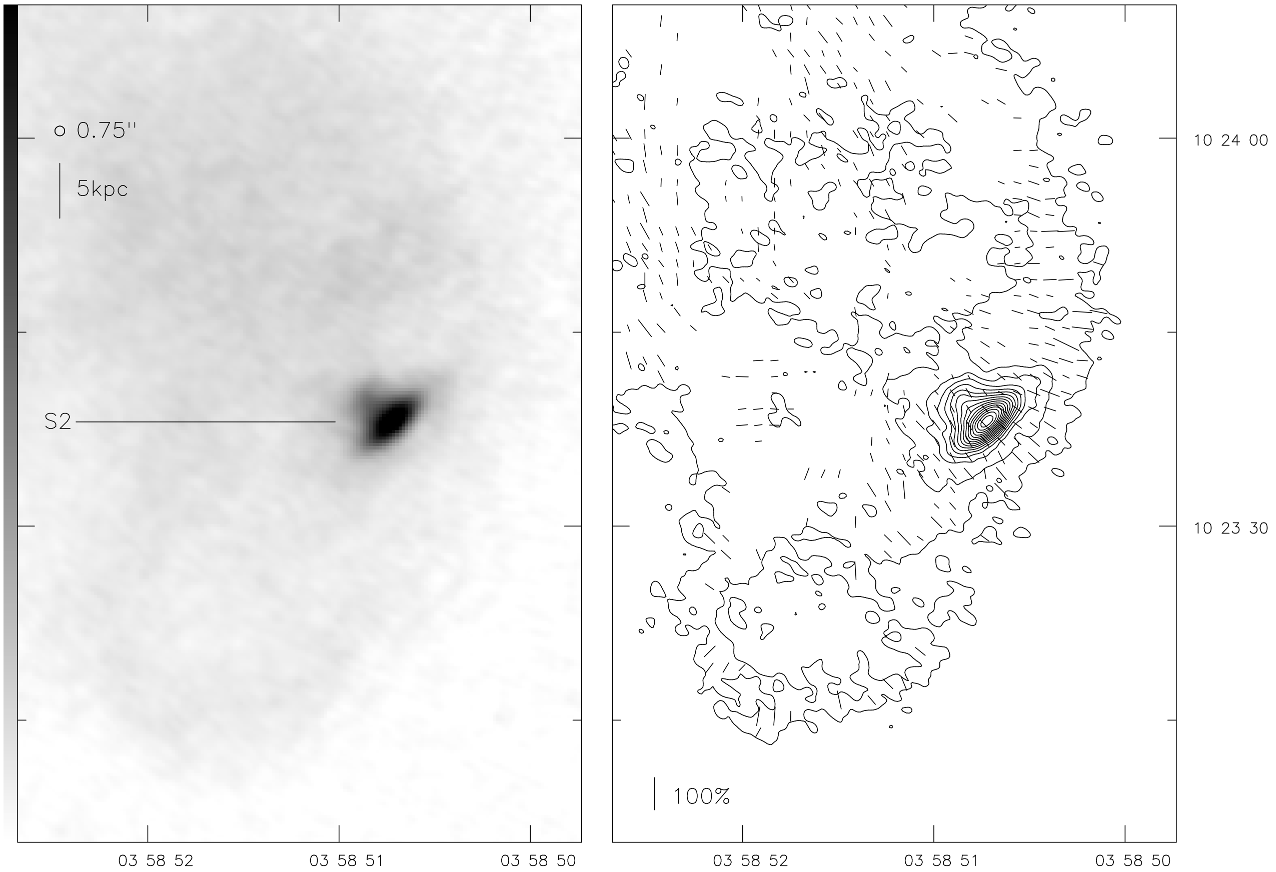

Figure 6. Sp hotspot of 3C98 at 0.75 arcsec resolution. (a) Linear greyscale; black is 2 mJy beam^{-1}. (b) Linear contours at $0.15 \times (-2, -1, 1, 2, 3, 4, \ldots)$ mJy beam^{-1}. Negative contours are dashed.

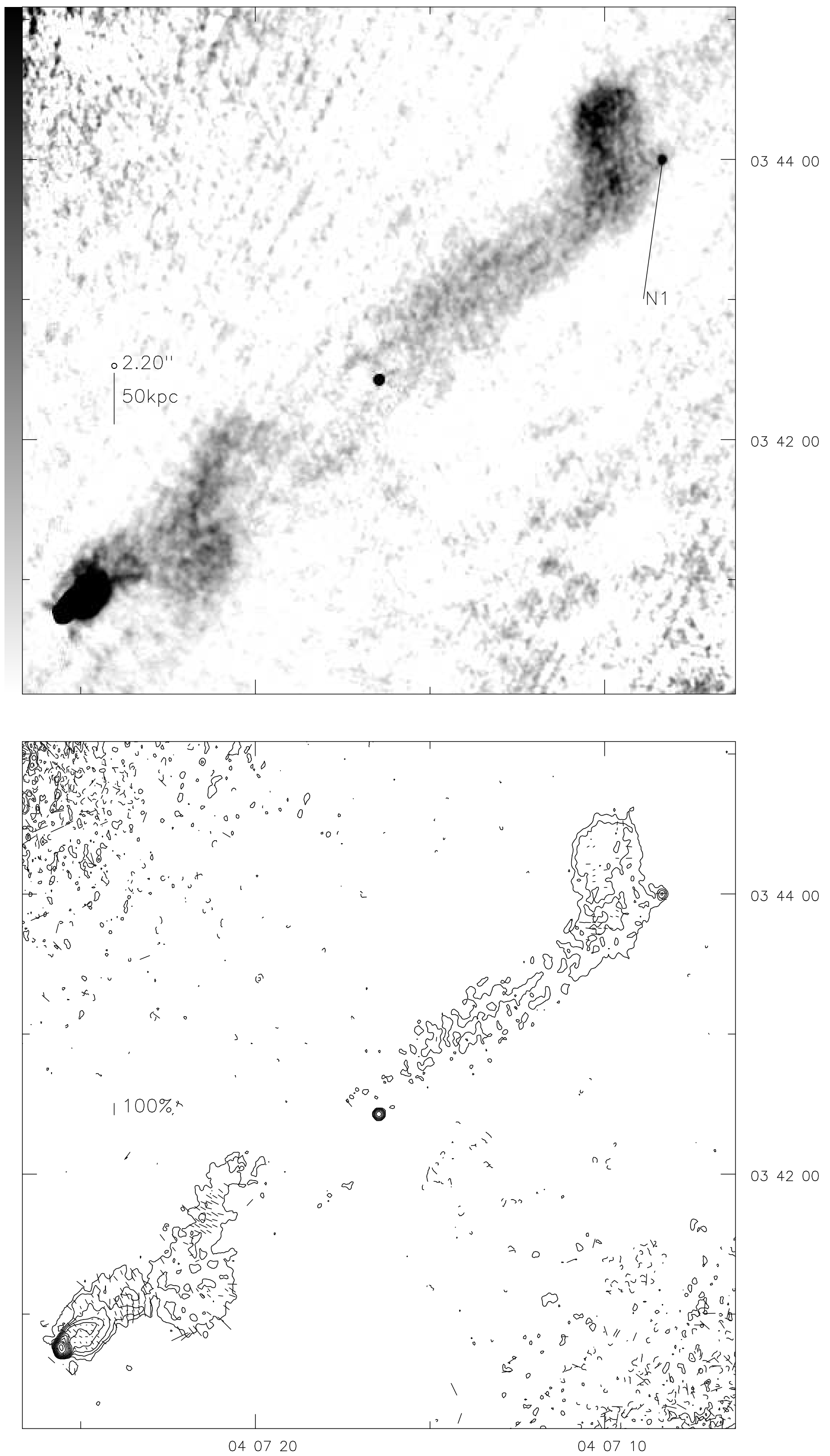

Figure 7. 3C105 at 2.20 arcsec resolution. (a) Linear greyscale; black is 1 mJy beam^{-1}. (b) Contours at $0.3 \times (-2, -1, 1, 2, 4, \ldots)$ mJy beam^{-1}. Negative contours are dashed.

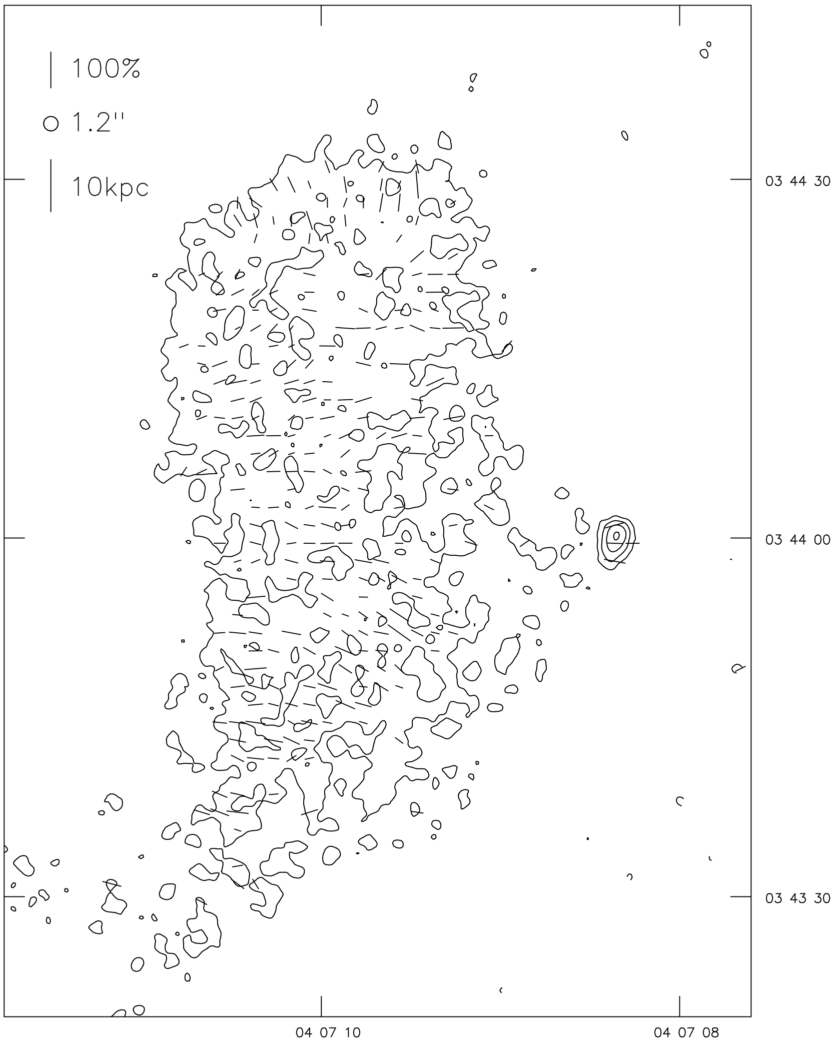

Figure 8. Np hotspot of 3C105 at 1.20 arcsec resolution. Contours at $0.2 \times (-2, -1, 1, 2, 4, \ldots)$ mJy beam^{-1}. Negative contours are dashed.

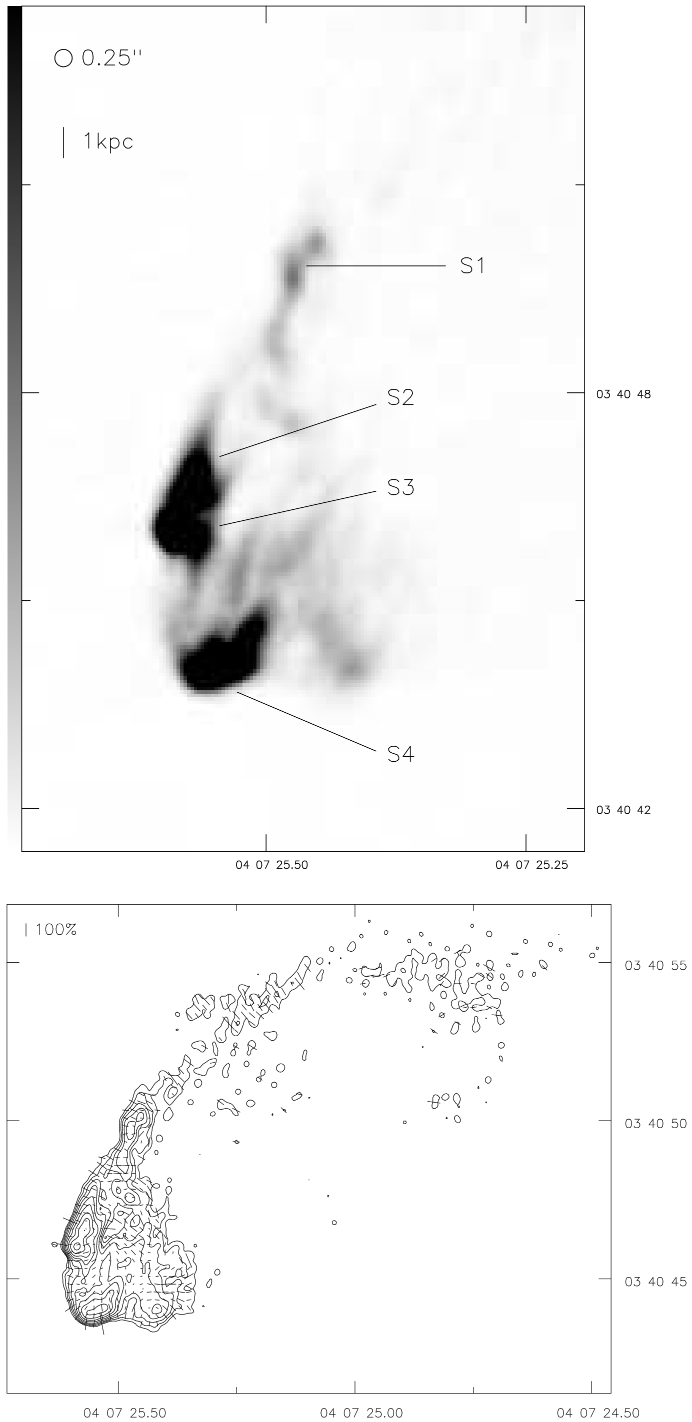

Figure 9. Sf hotspot of 3C105 at 0.25 arcsec resolution. (a) Linear greyscale; black is 10 mJy beam^{-1}. (b) Contours at $0.2 \times (-2, -1, 1, 2, 4, \ldots)$ mJy beam^{-1}. Negative contours are dashed.

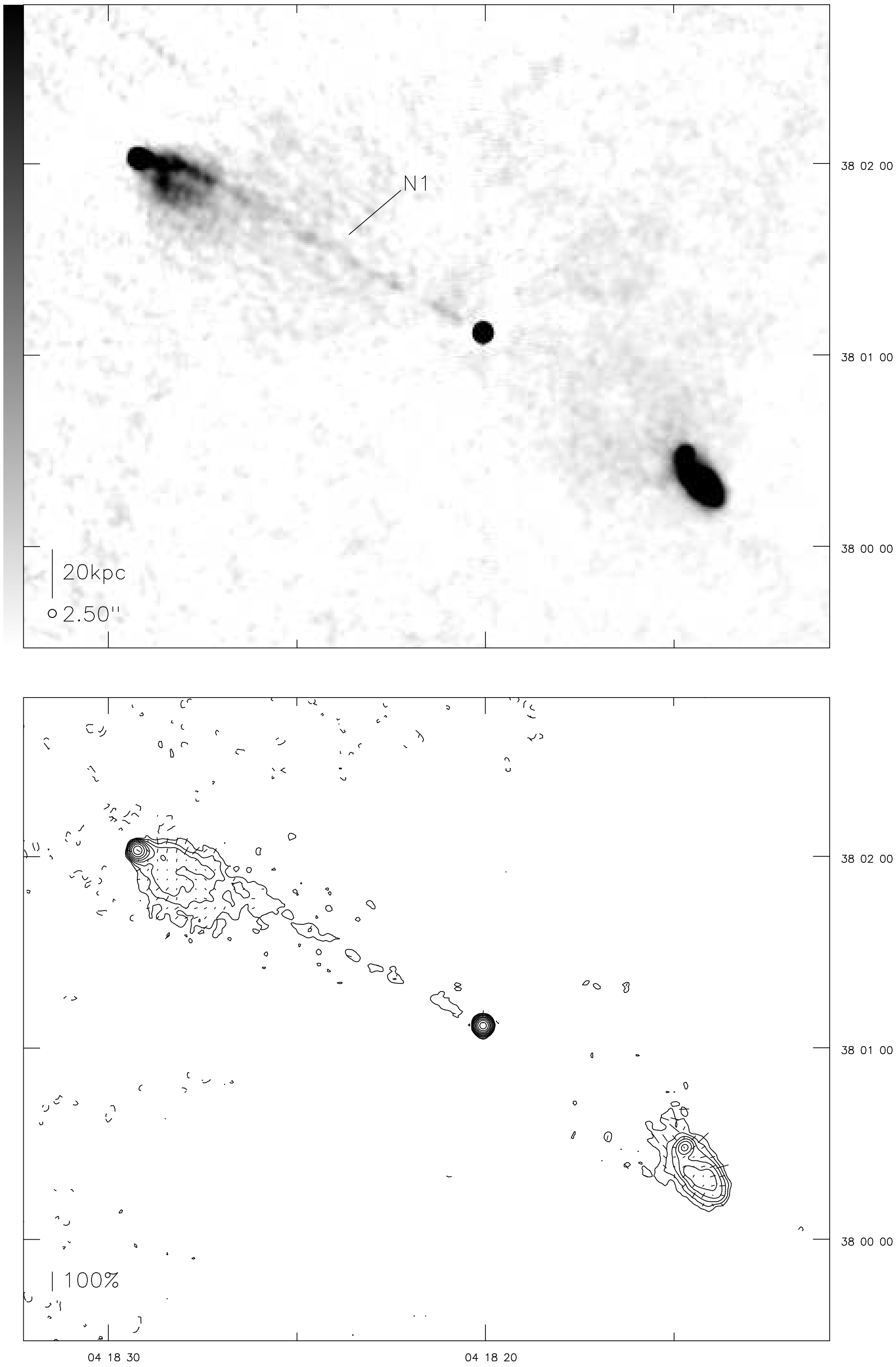

Figure 10. 3C111 at 2.50 arcsec resolution. (a) Linear greyscale; black is 10 mJy beam^{-1}. (b) Contours at $1.5 \times (-2, -1, 1, 2, 4, \ldots)$ mJy beam^{-1}. Negative contours are dashed.

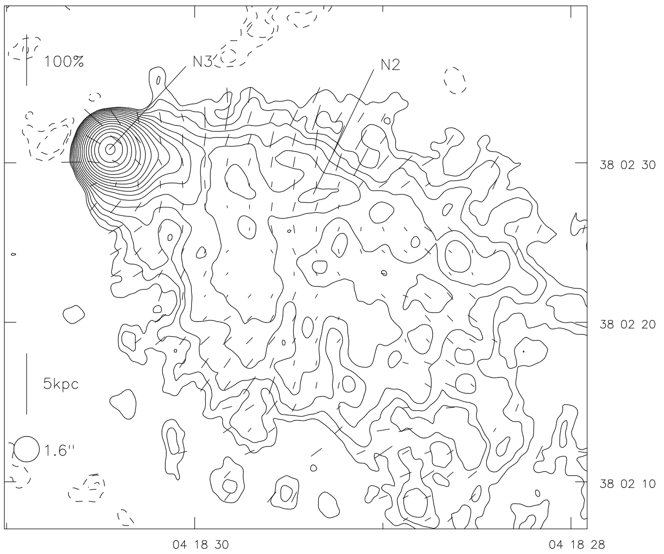

Figure 11. Nf hotspot of 3C111 at 1.60 arcsec resolution. Contours at $1 \times (-\sqrt{2}, -1, 1, \sqrt{2}, 2, 2\sqrt{2}, \ldots)$ mJy beam^{-1}. Negative contours are dashed.

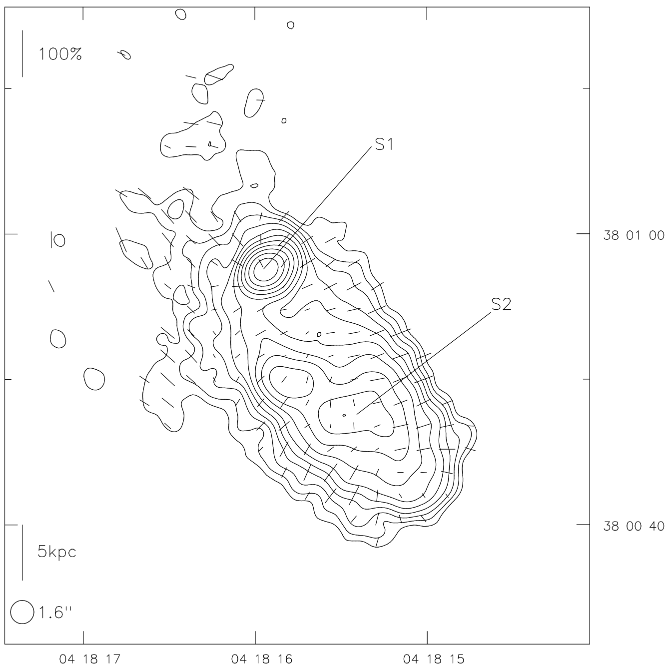

Figure 13. Sp hotspot of 3C111 at 1.60 arcsec resolution. Contours at $1 \times (-\sqrt{2}, -1, 1, \sqrt{2}, 2, 2\sqrt{2}, \ldots)$ mJy beam^{-1}. Negative contours are dashed.

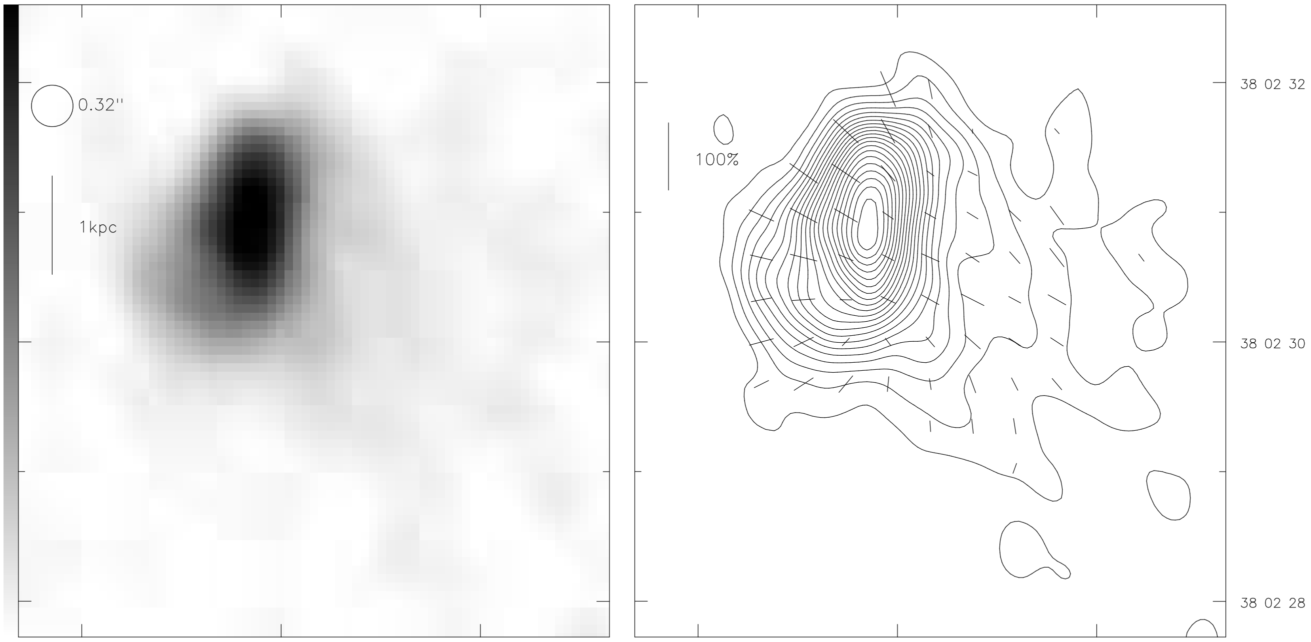

Figure 12. Nf hotspot of 3C111 at 0.32 arcsec resolution. (a) Linear greyscale; black is 30 mJy beam^{-1}. (b) Linear contours at $1.5 \times (-2, -1, 1, 2, 3, 4, \ldots)$ mJy beam^{-1}. Negative contours are dashed.

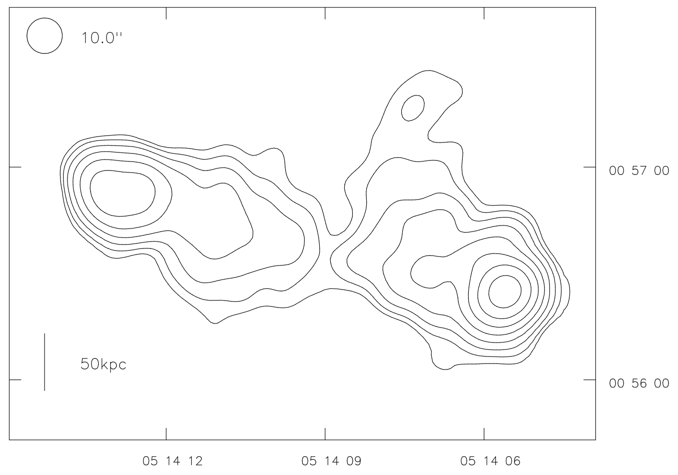

Figure 14. 3C135 at 10.00 arcsec resolution. Contours at $0.8 \times (-2, -1, 1, 2, 4, \ldots)$ mJy beam^{-1}. Negative contours are dashed.

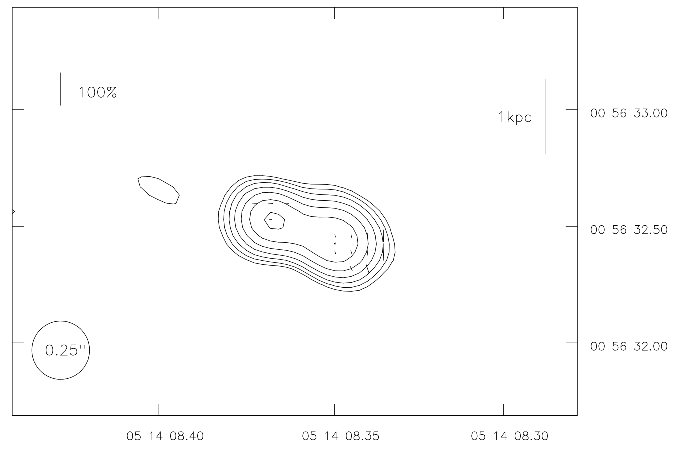

Figure 17. Core of 3C135 at 0.25 arcsec resolution. Contours at $130 \times (-\sqrt{2}, -1, 1, \sqrt{2}, 2, 2\sqrt{2}, \ldots)$ μJy beam^{-1}. Negative contours are dashed. Polarization vectors are four times oversampled.

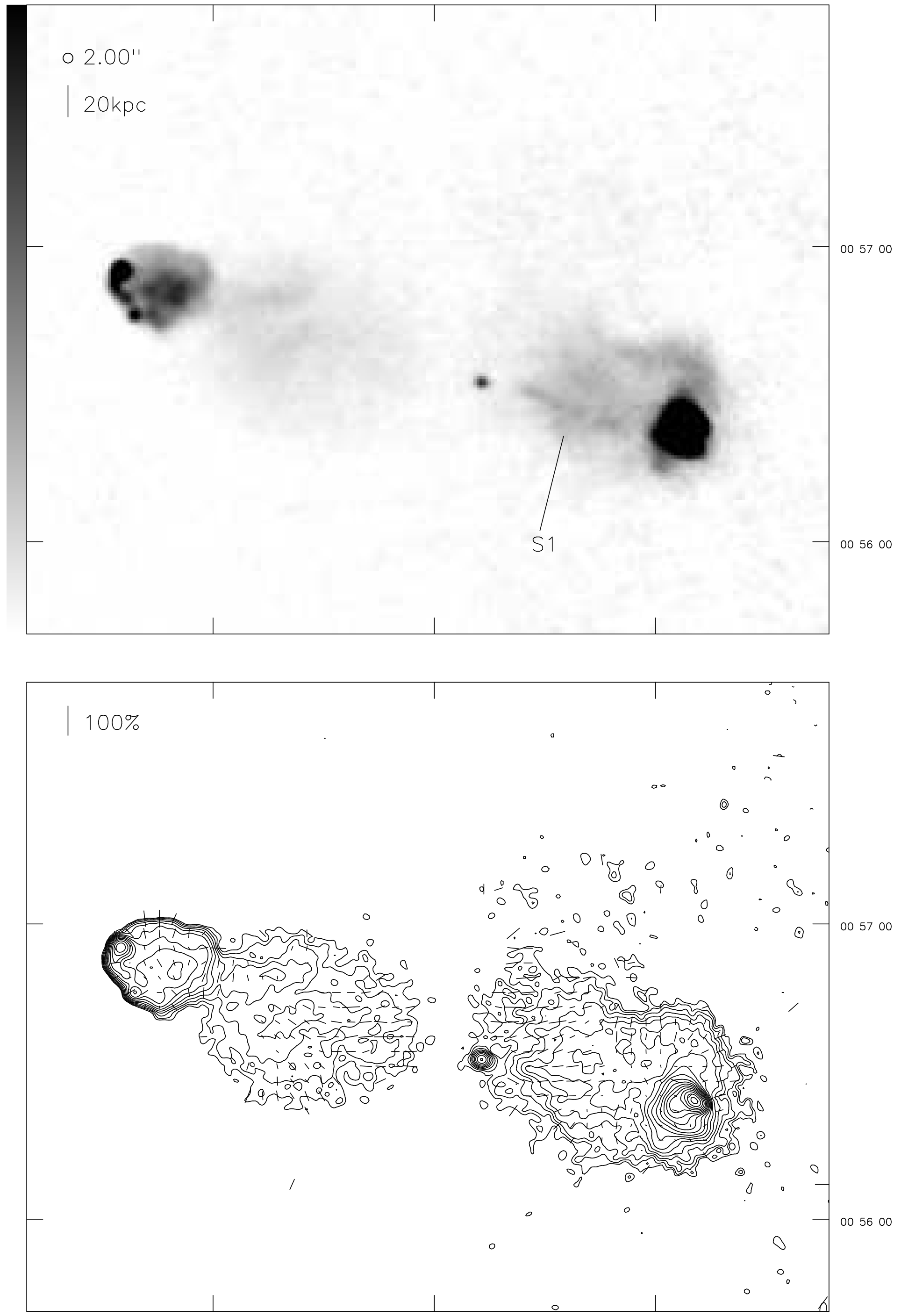

Figure 15. 3C135 at 2.00 arcsec resolution. (a) Linear greyscale; black is 3 mJy beam^{-1}. (b) Contours at $0.15 \times (-2, -1, 1, 2, 4, \ldots)$ mJy beam^{-1}. Negative contours are dashed.

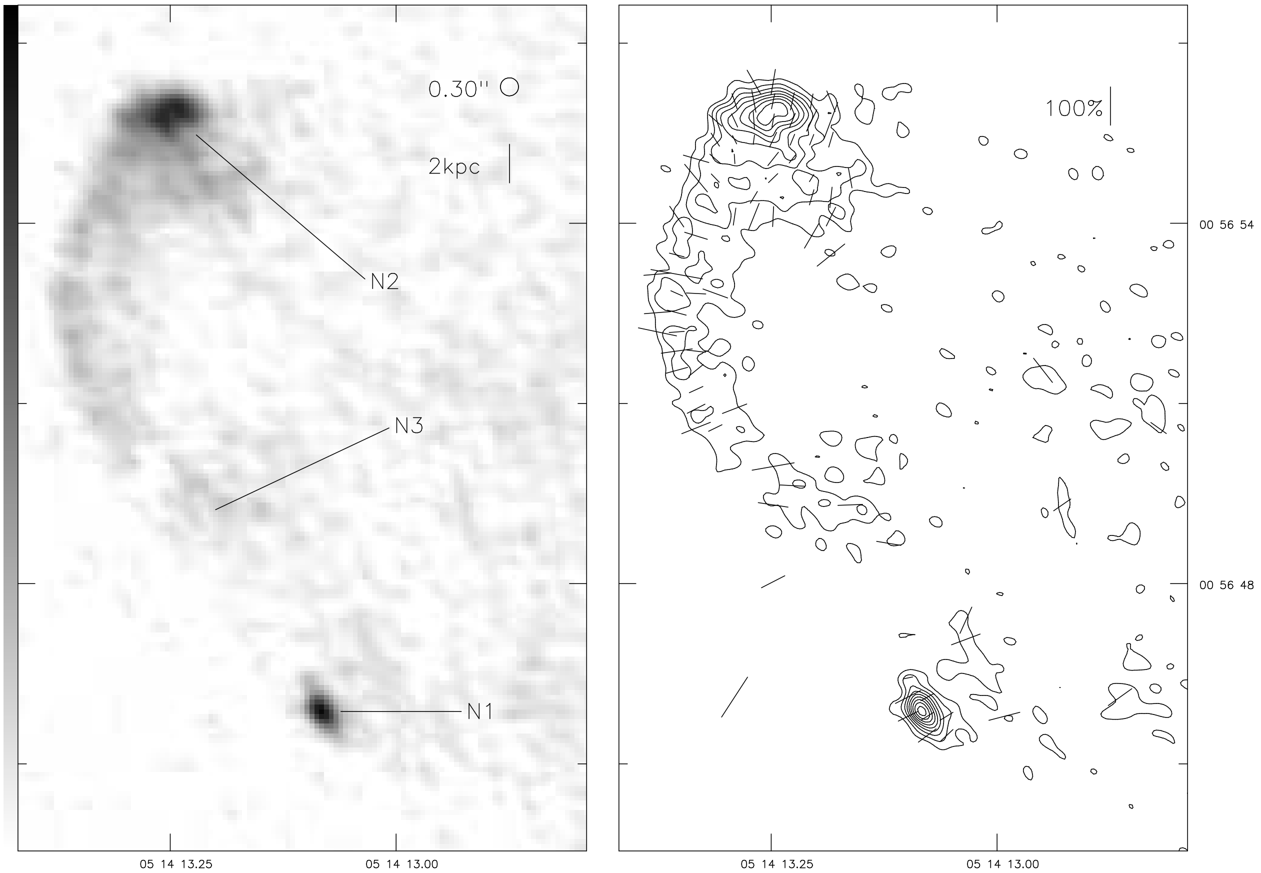

Figure 16. Nf hotspot of 3C135 at 0.30 arcsec resolution. (a) Linear greyscale; black is 0.8 mJy beam^{-1}. (b) Linear contours at $80 \times (-2, -1, 1, 2, 3, 4, \ldots)$ μJy beam^{-1}. Negative contours are dashed.

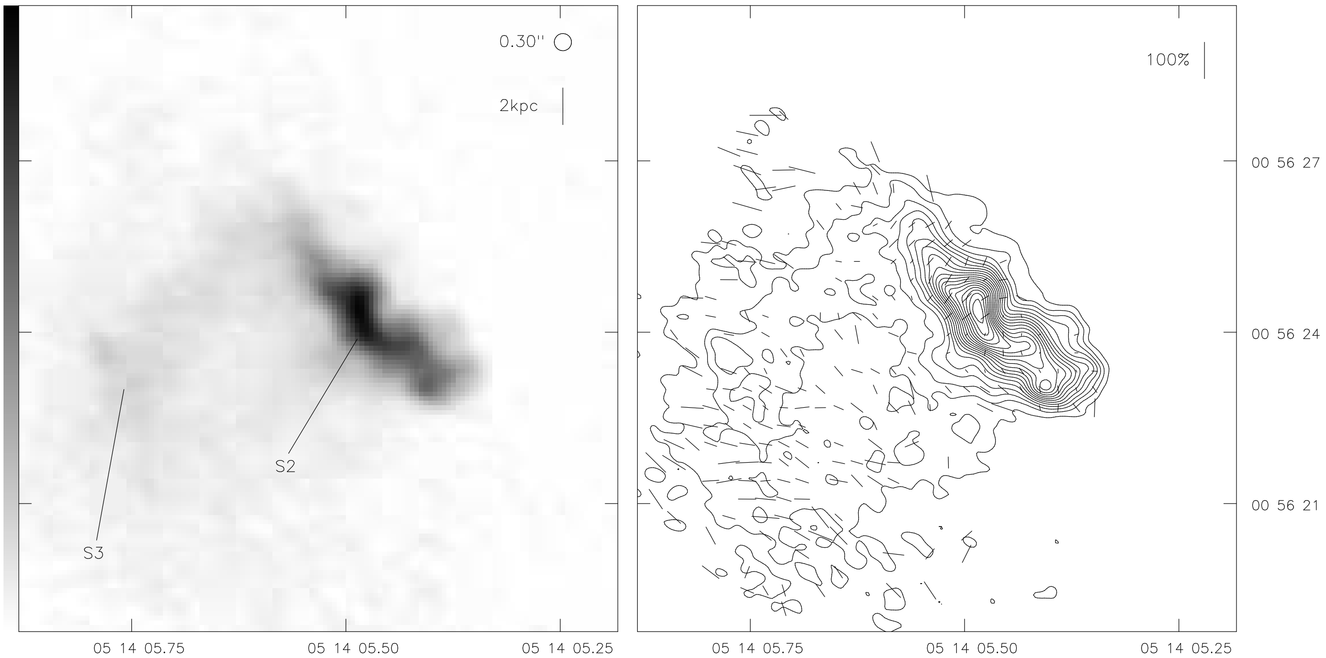

Figure 18. Sp hotspot of 3C135 at 0.30 arcsec resolution. (a) Linear greyscale; black is 4 mJy beam^{-1}. (b) Linear contours at $0.2 \times (-2, -1, 1, 2, 3, 4, \ldots)$ mJy beam^{-1}. Negative contours are dashed.

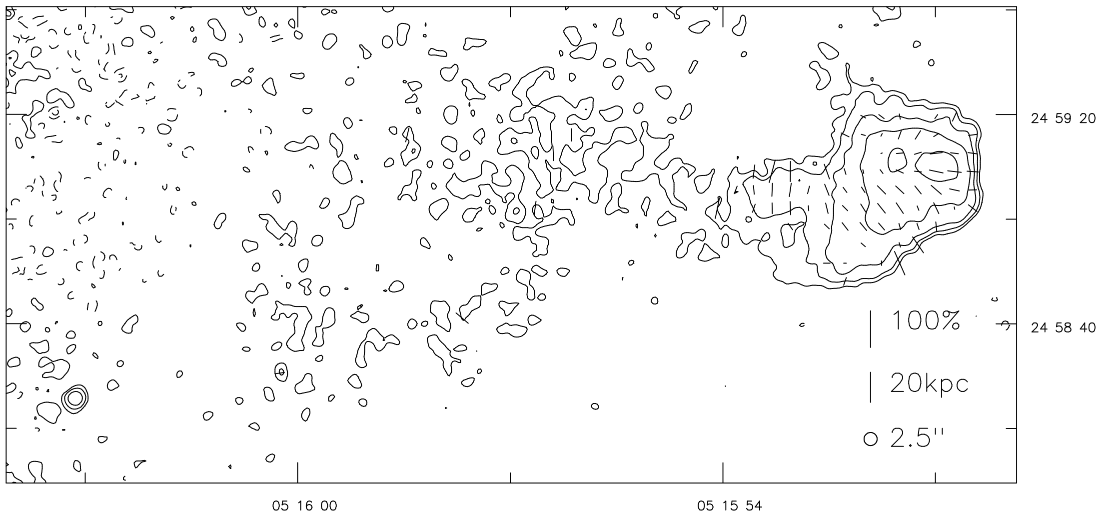

Figure 19. Np lobe of 3C136.1 at 2.50 arcsec resolution. Contours at $0.2 \times (-2, -1, 1, 2, 4, \ldots)$ mJy beam^{-1}. Negative contours are dashed.

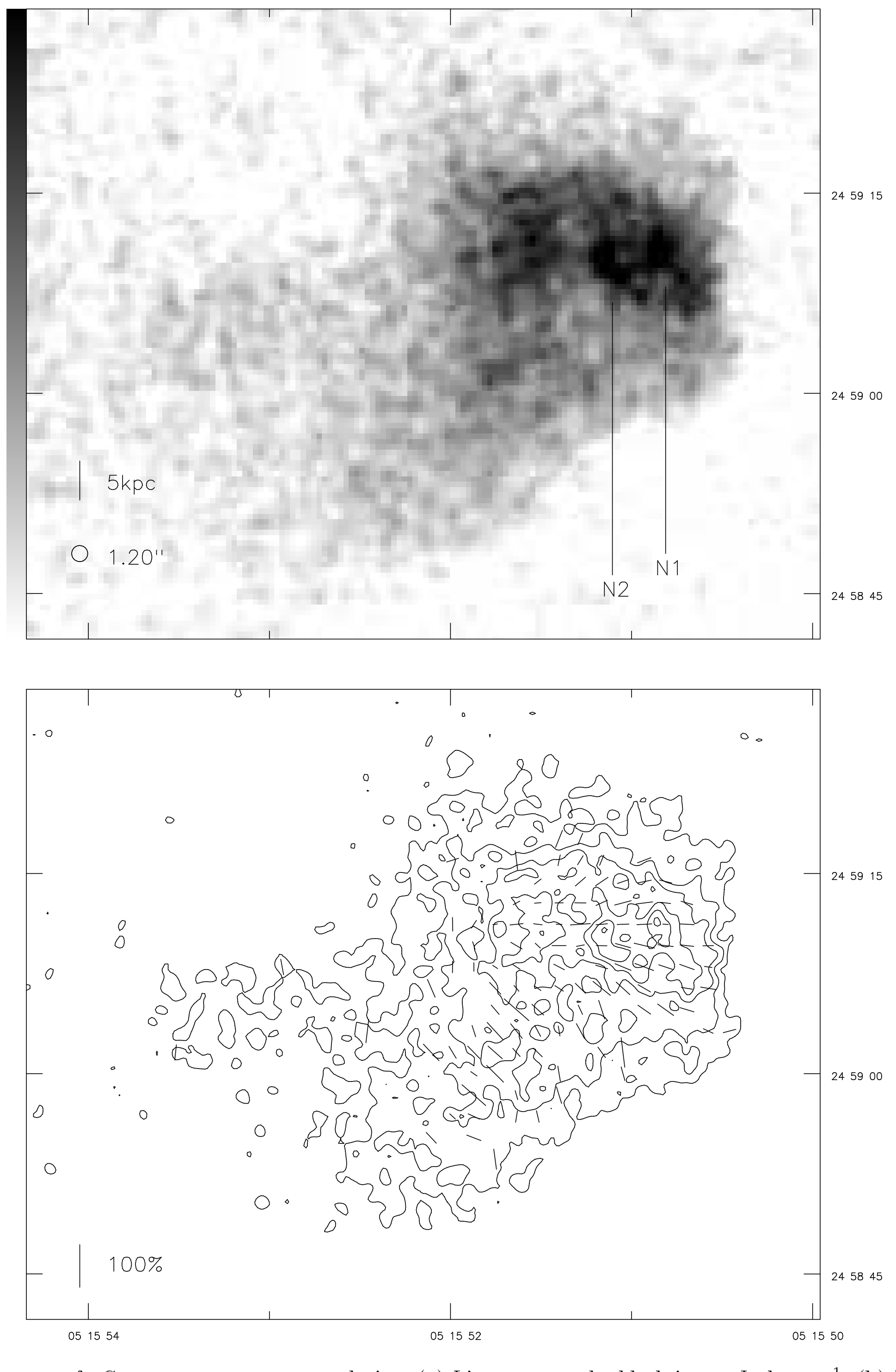

Figure 20. Np hotspot of 3C136.1 at 1.20 arcsec resolution. (a) Linear greyscale; black is 1 mJy beam^{-1}. (b) Linear contours at $0.2 \times (-2, -1, 1, 2, 3, 4 \ldots)$ mJy beam^{-1}. Negative contours are dashed.

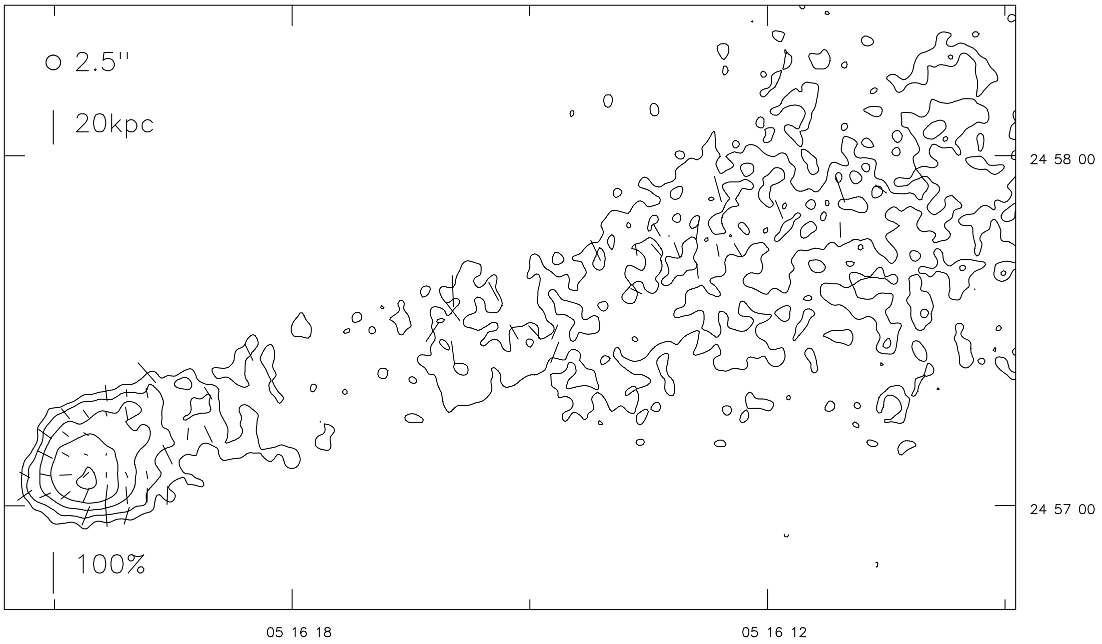

Figure 21. Sf lobe of 3C136.1 at 2.50 arcsec resolution. Contours at $0.2 \times (-2, -1, 1, 2, 4, \ldots)$ mJy beam^{-1}. Negative contours are dashed.

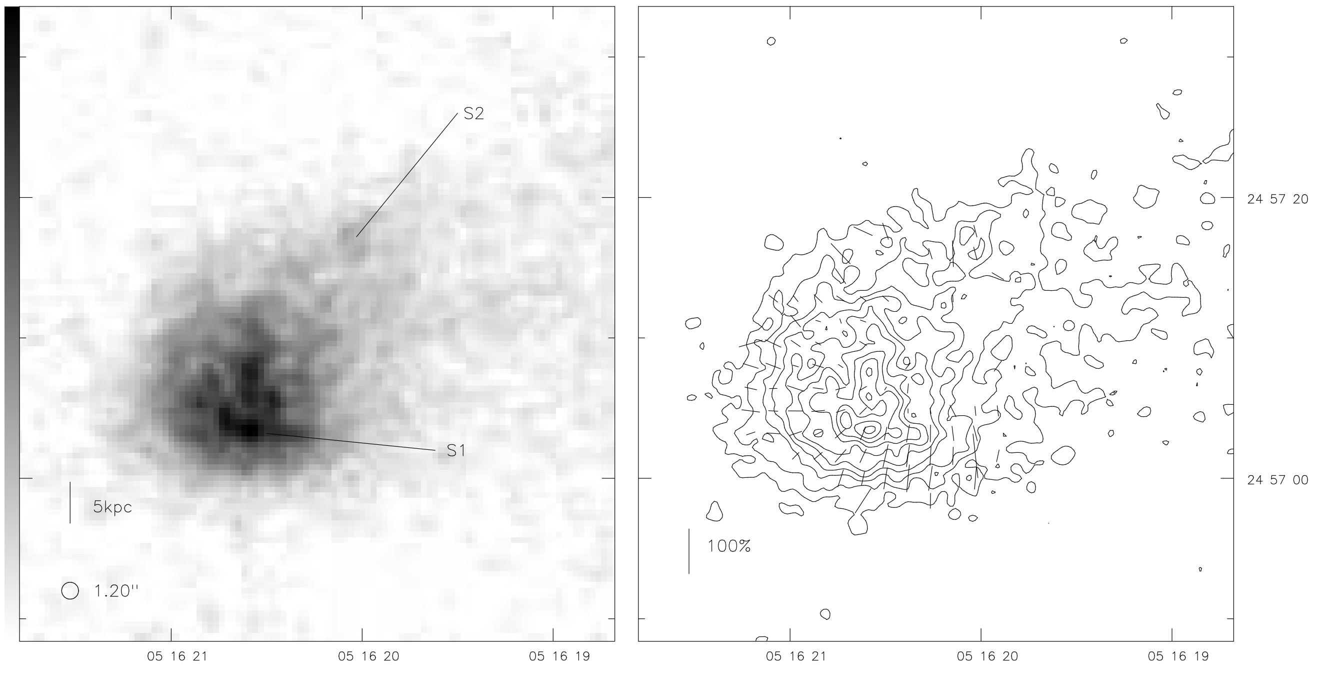

Figure 22. Sf hotspot of 3C136.1 at 1.20 arcsec resolution. (a) Linear greyscale; black is 1 mJy beam^{-1}. (b) Linear contours at $0.1 \times (-2, -1, 1, 2, 3, 4 \ldots)$ mJy beam^{-1}. Negative contours are dashed.

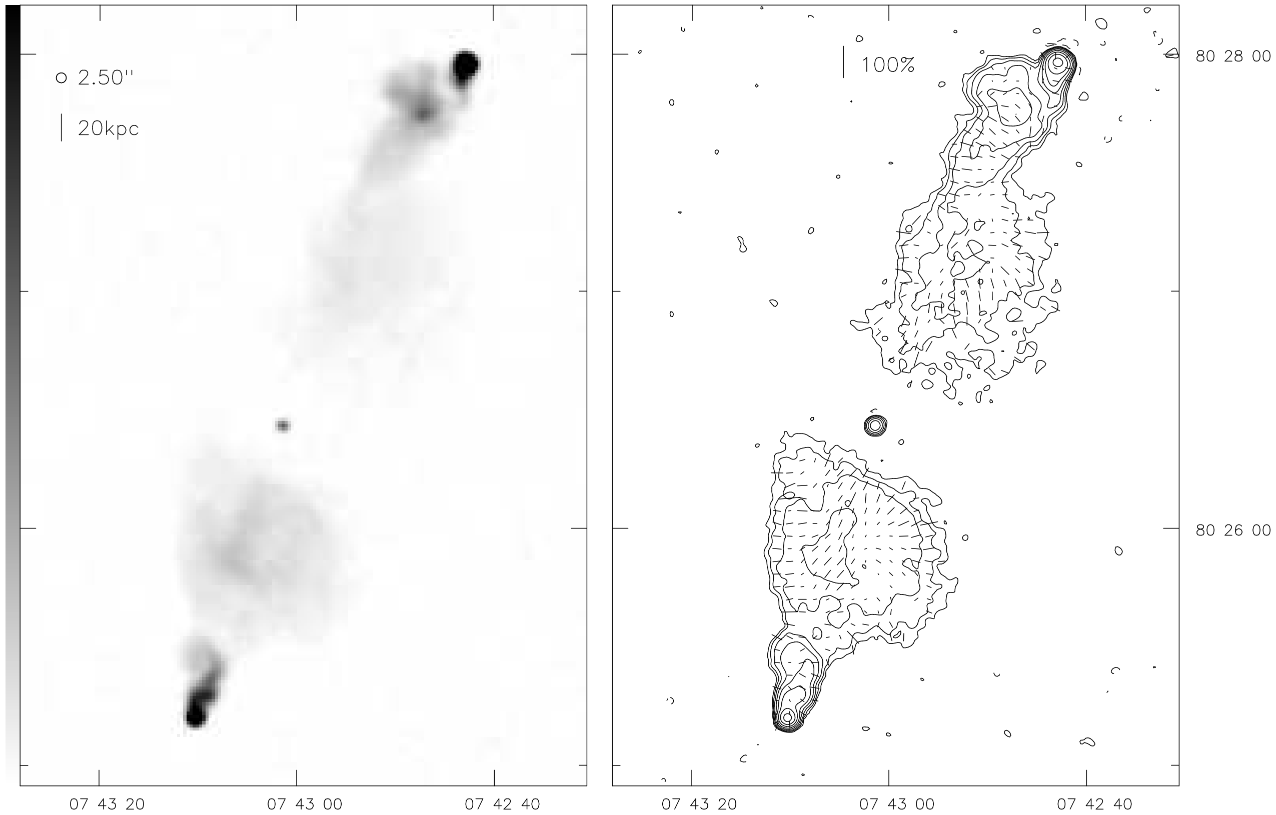

Figure 23. 3C184.1 at 2.50 arcsec resolution. (a) Linear greyscale; black is 10 mJy beam^{-1}. (b) Contours at $0.2 \times (-2, -1, 1, 2, 4, \ldots)$ mJy beam^{-1}. Negative contours are dashed.

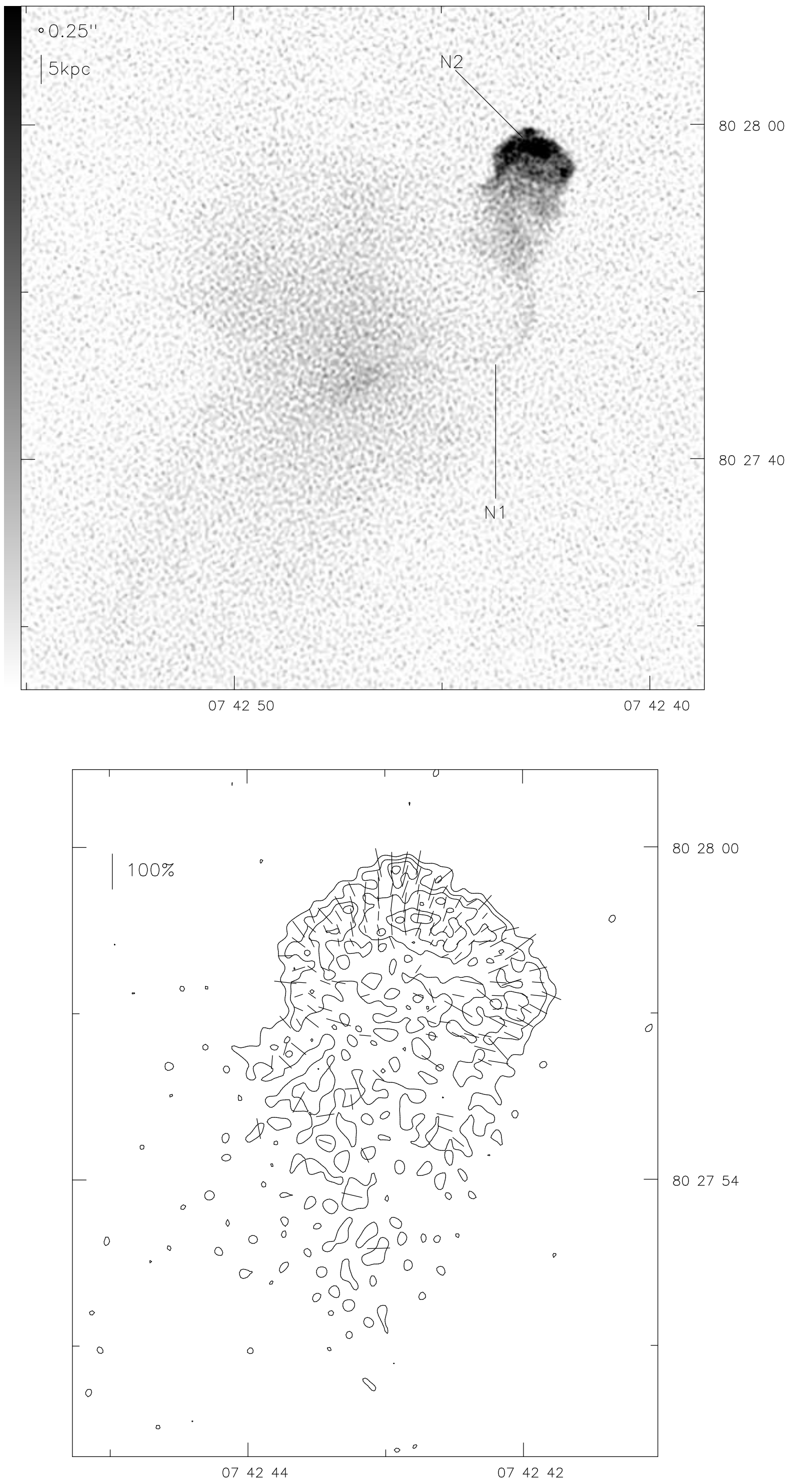

Figure 24. Np hotspot of 3C184.1 at 0.25 arcsec resolution. (a) Linear greyscale; black is 0.5 mJy beam^{-1}. (b) Linear contours at $0.15 \times (-2, -1, 1, 2, 3, 4, \ldots)$ mJy beam^{-1}. Negative contours are dashed.

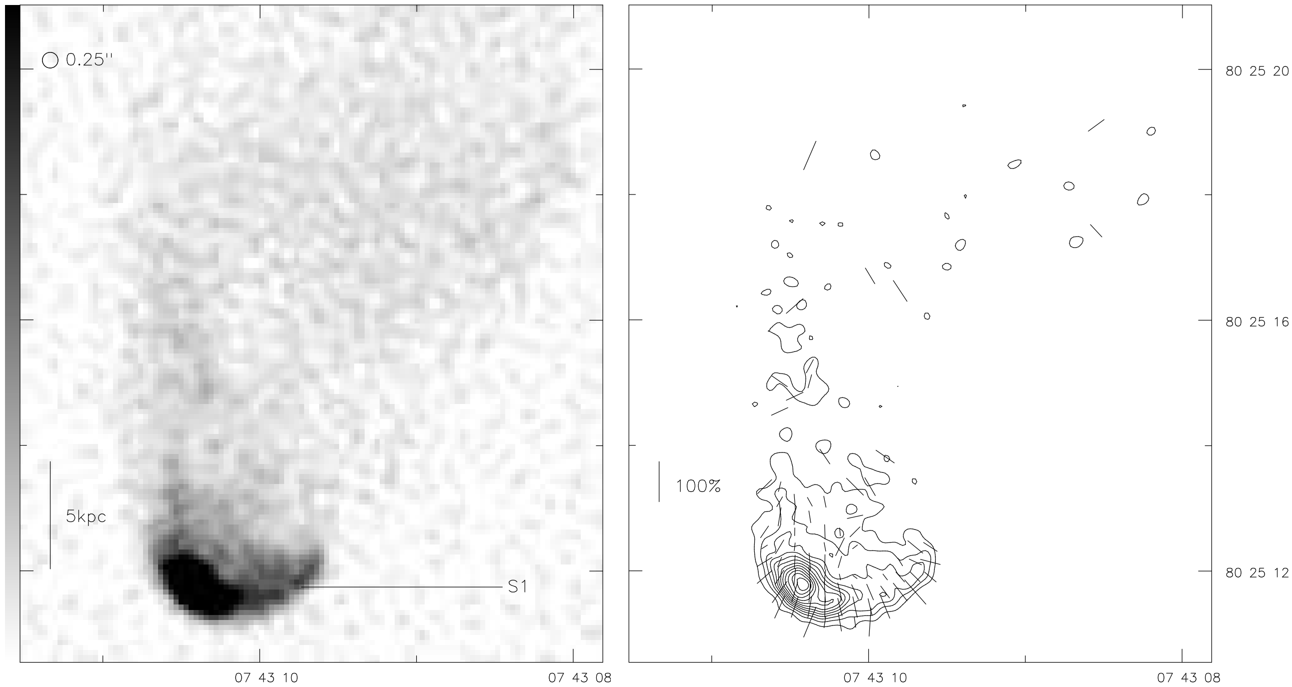

Figure 25. Sf hotspot of 3C184.1 at 0.25 arcsec resolution. (a) Linear greyscale; black is 1 mJy beam^{-1}. (b) Linear contours at $0.2 \times (-2, -1, 1, 2, 3, 4, \ldots)$ mJy beam^{-1}. Negative contours are dashed.

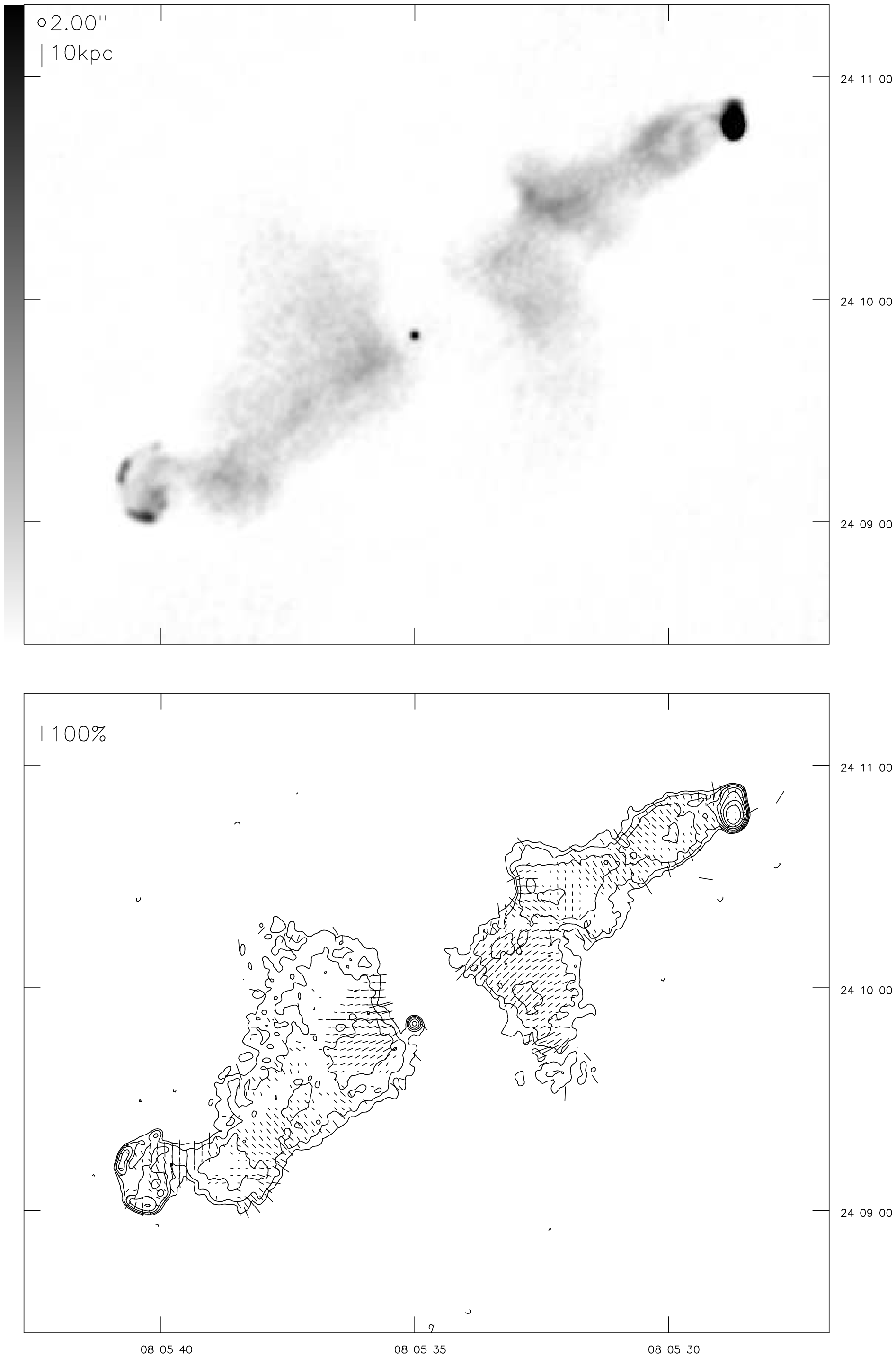

Figure 26. 3C192 at 2.00 arcsec resolution. (a) Linear greyscale; black is 4 mJy beam^{-1}. (b) Contours at $0.2 \times (-2, -1, 1, 2, 4, \ldots)$ mJy beam^{-1}. Negative contours are dashed.

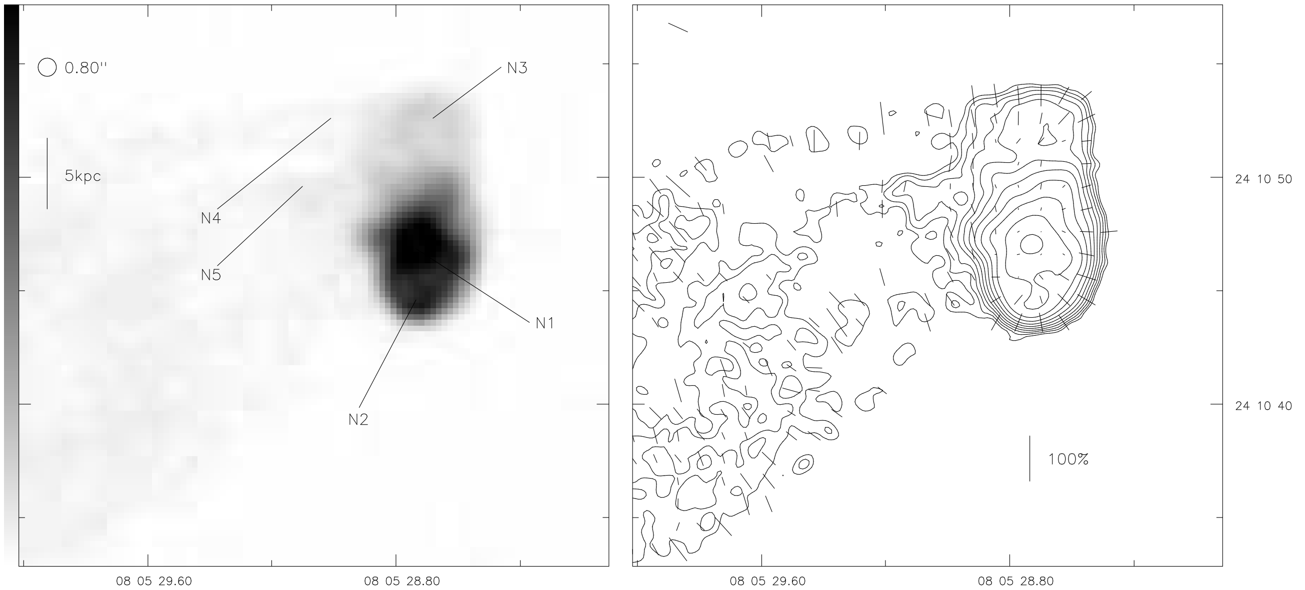

Figure 27. Np hotspot of 3C192 at 0.80 arcsec resolution. (a) Linear greyscale; black is 4 mJy beam^{-1}. (b) Contours at $0.15 \times (-\sqrt{2}, -1, 1, \sqrt{2}, 2, 2\sqrt{2}\ldots)$ mJy beam^{-1}. Negative contours are dashed.

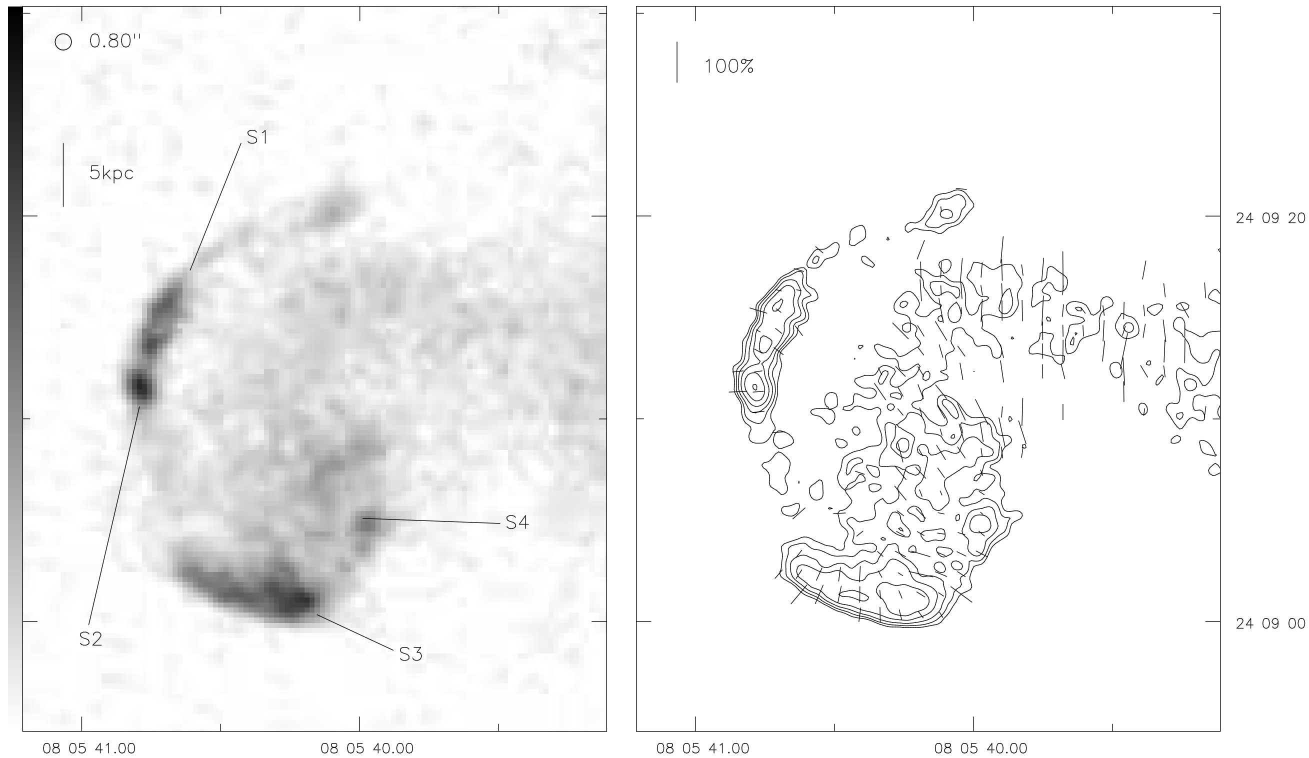

Figure 28. Sf hotspot of 3C192 at 0.80 arcsec resolution. (a) Linear greyscale; black is 1 mJy beam^{-1}. (b) Contours at $0.15 \times (-\sqrt{2}, -1, 1, \sqrt{2}, 2, 2\sqrt{2}\ldots)$ mJy beam^{-1}. Negative contours are dashed.

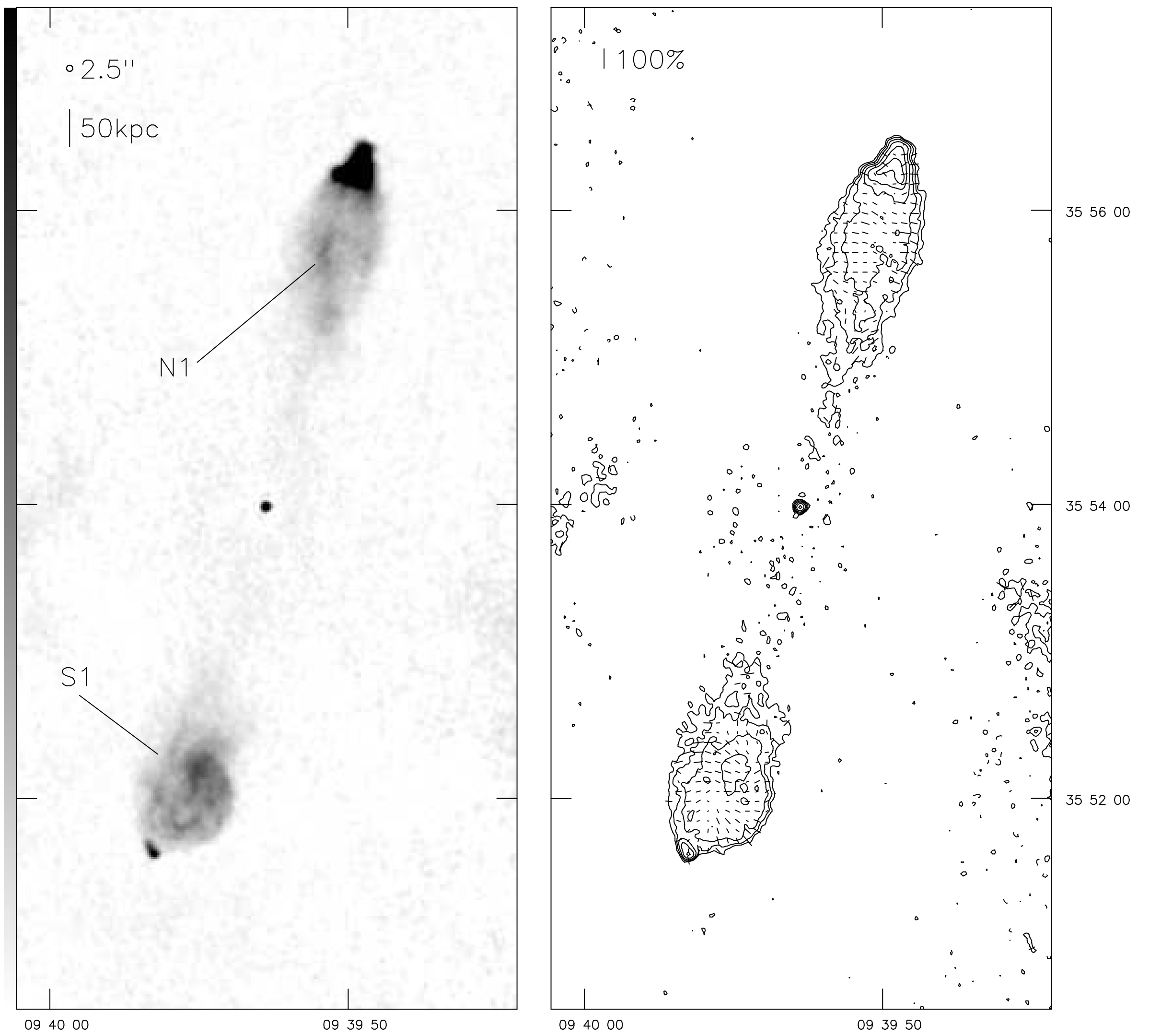

Figure 29. 3C223 at 2.50 arcsec resolution. (a) Linear greyscale; black is 3 mJy beam^{-1}. (b) Contours at $0.2 \times (-2, -1, 1, 2, 4, \ldots)$ mJy beam^{-1}. Negative contours are dashed.

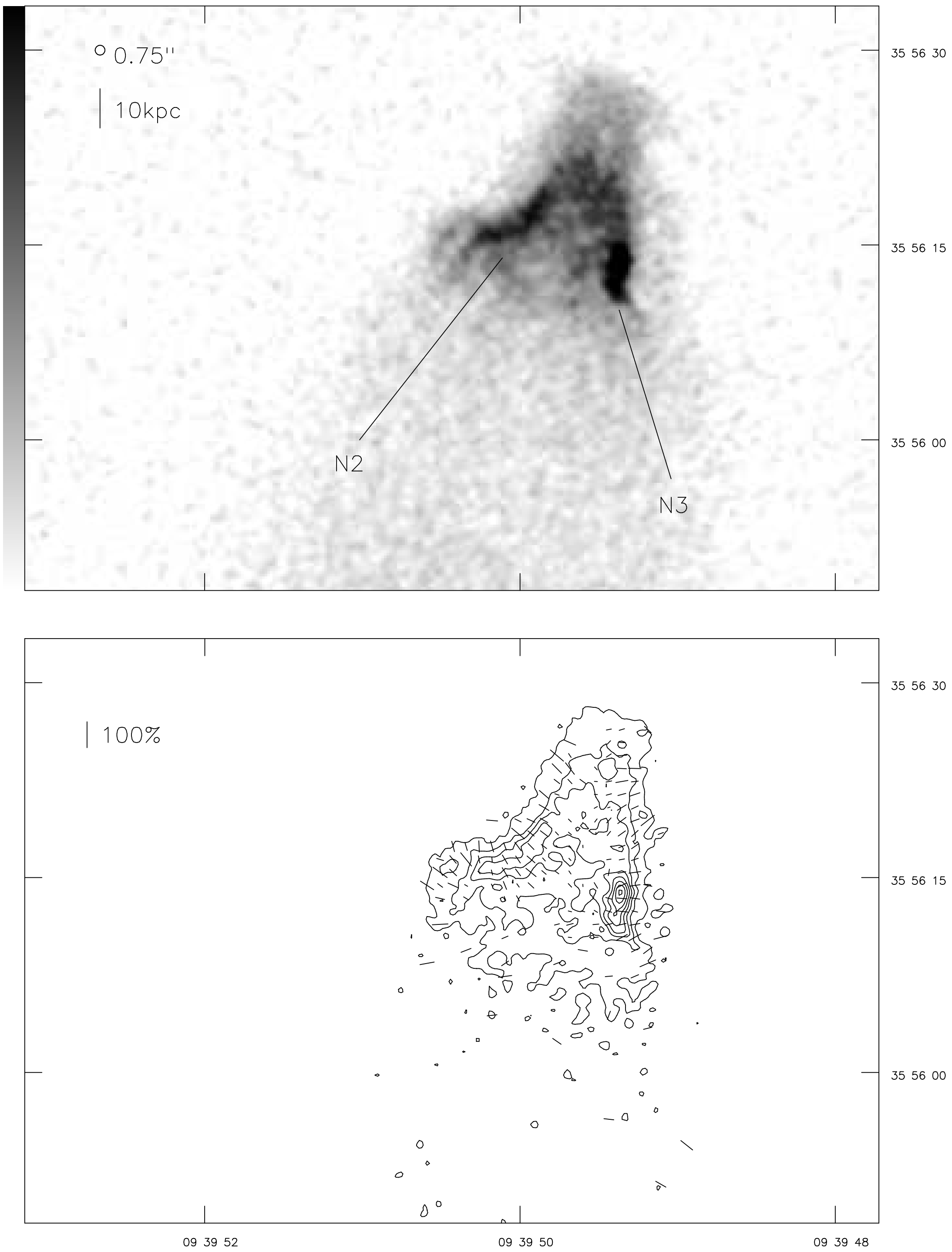

Figure 30. Np hotspot of 3C223 at 0.75 arcsec resolution. (a) Linear greyscale; black is 1 mJy beam^{-1}. (b) Linear contours at $0.2 \times (-2, -1, 1, 2, 3, 4, \ldots)$ mJy beam^{-1}. Negative contours are dashed.

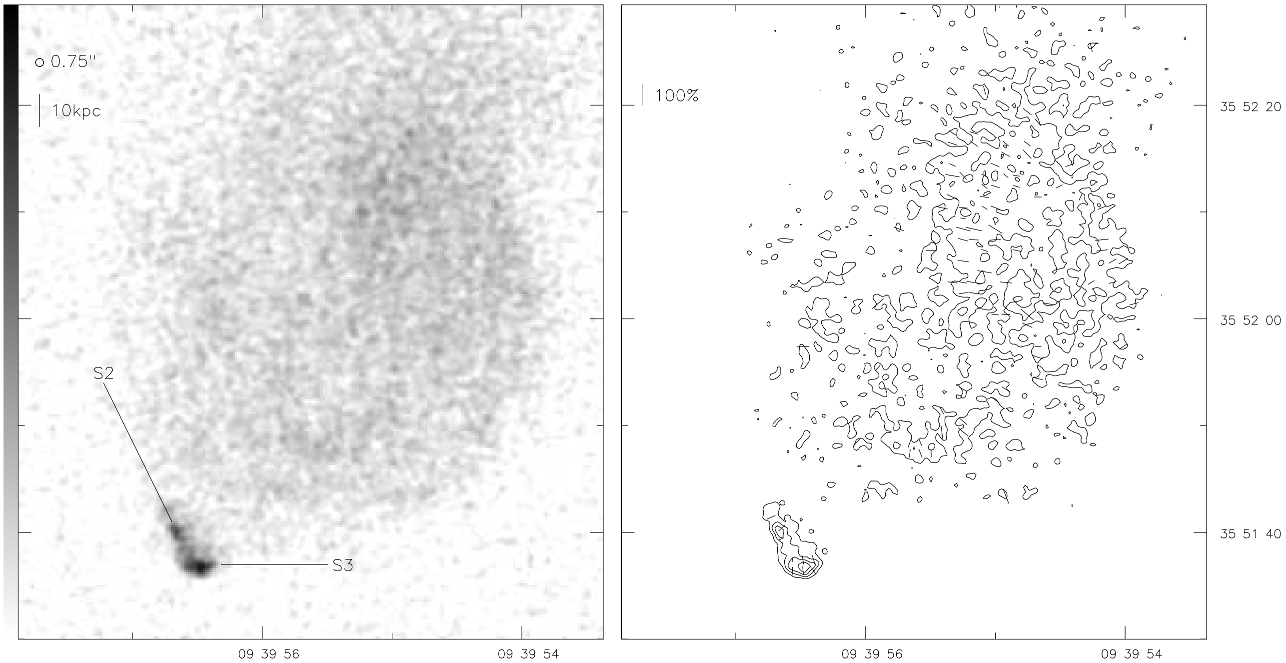

Figure 31. Sf hotspot of 3C223 at 0.75 arcsec resolution. (a) Linear greyscale; black is 0.8 mJy beam^{-1}. (b) Linear contours at $0.15 \times (-2, -1, 1, 2, 3, 4, \ldots)$ mJy beam^{-1}. Negative contours are dashed.

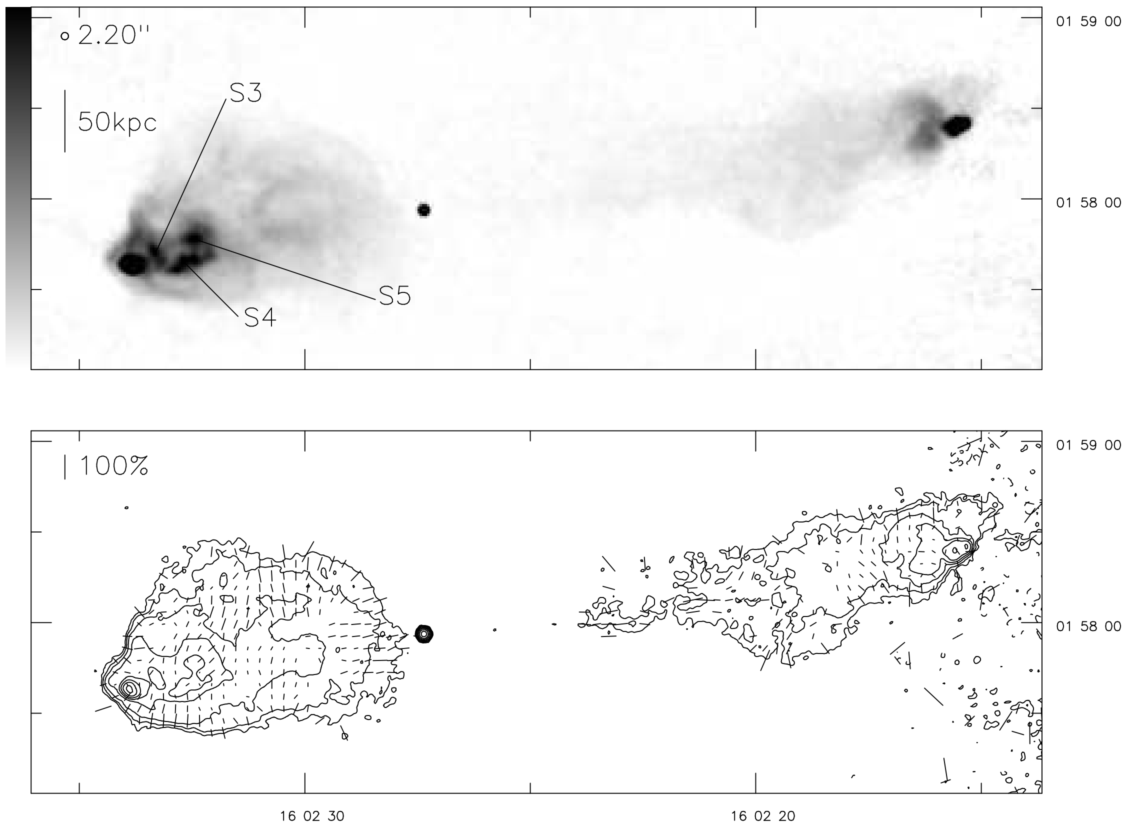

Figure 32. 3C327 at 2.20 arcsec resolution. (a) Linear greyscale; black is 5 mJy beam^{-1}. (b) Contours at $0.25 \times (-2, -1, 1, 2, 4, \ldots)$ mJy beam^{-1}. Negative contours are dashed. The higher noise at the W end of the map is due to primary beam attenuation (the pointing centre was at the core).

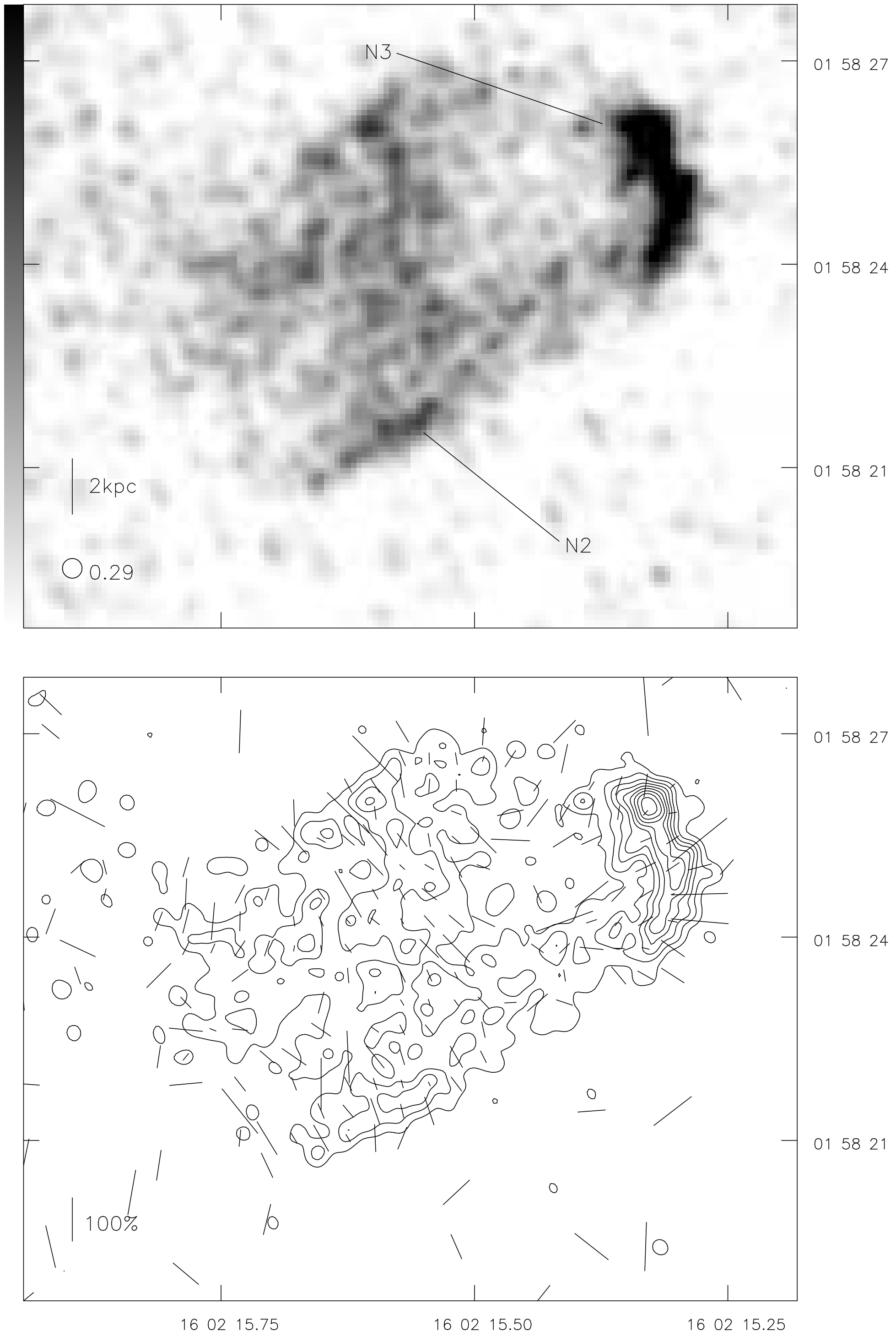

Figure 33. Np hotspot of 3C327 at 0.29 arcsec resolution. (a) Linear greyscale; black is 1 mJy beam^{-1}. (b) Linear contours at $0.2 \times (-2, -1, 1, 2, 3, 4, \ldots)$ mJy beam^{-1}. Negative contours are dashed.

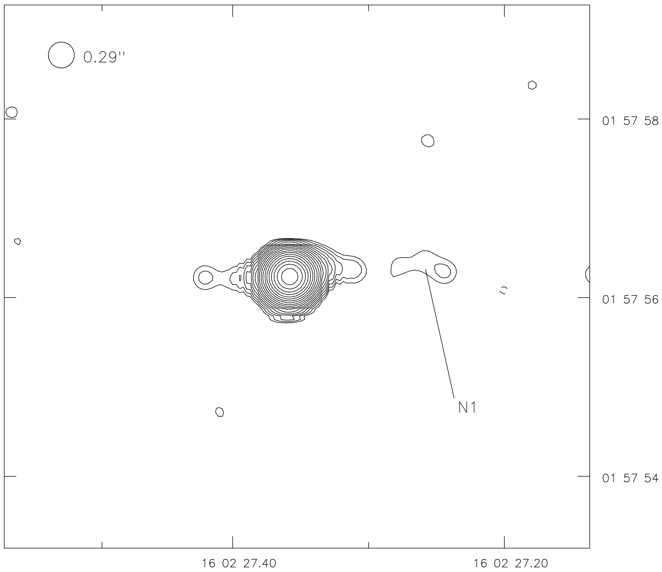

Figure 34. Core of 3C327 at 0.29 arcsec resolution. Contours at $50 \times (-\sqrt{2}, -1, 1, \sqrt{2}, 2, 2\sqrt{2}, \ldots)$ μJy beam^{-1}. Negative contours are dashed.

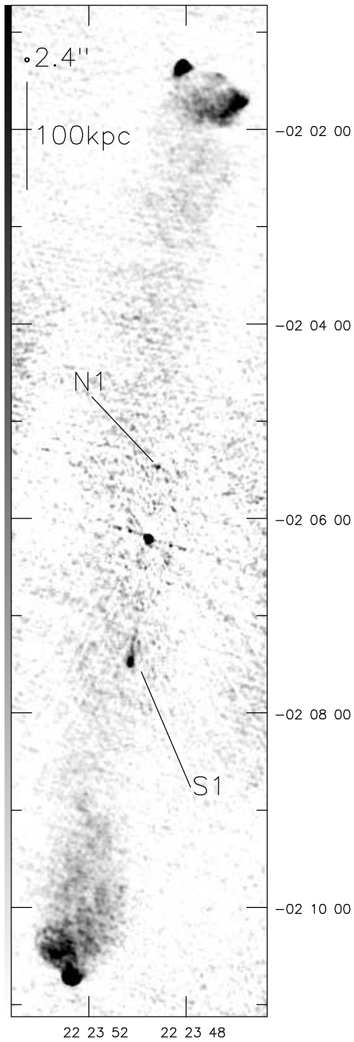

Figure 36. 3C445 at 2.40 arcsec resolution. Linear greyscale; black is 1 mJy beam^{-1}. Increased noise near the centre of the map is due to primary beam attenuation.

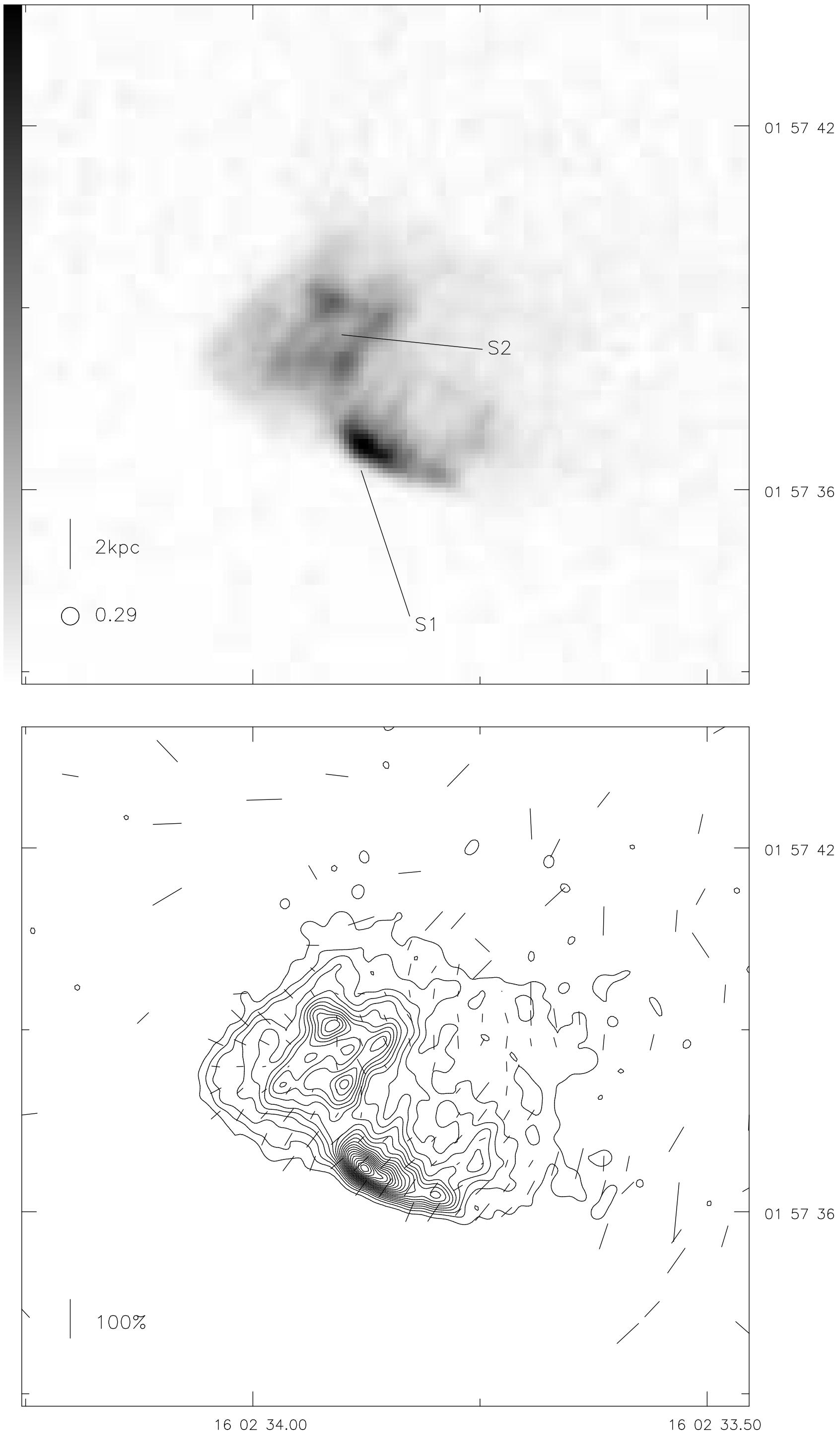

Figure 35. Sf hotspot of 3C327 at 0.29 arcsec resolution. (a) Linear greyscale; black is 4 mJy beam^{-1}. (b) Contours at $0.2 \times (-2, -1, 1, 2, 3, 4, \ldots)$ mJy beam^{-1}. Negative contours are dashed.

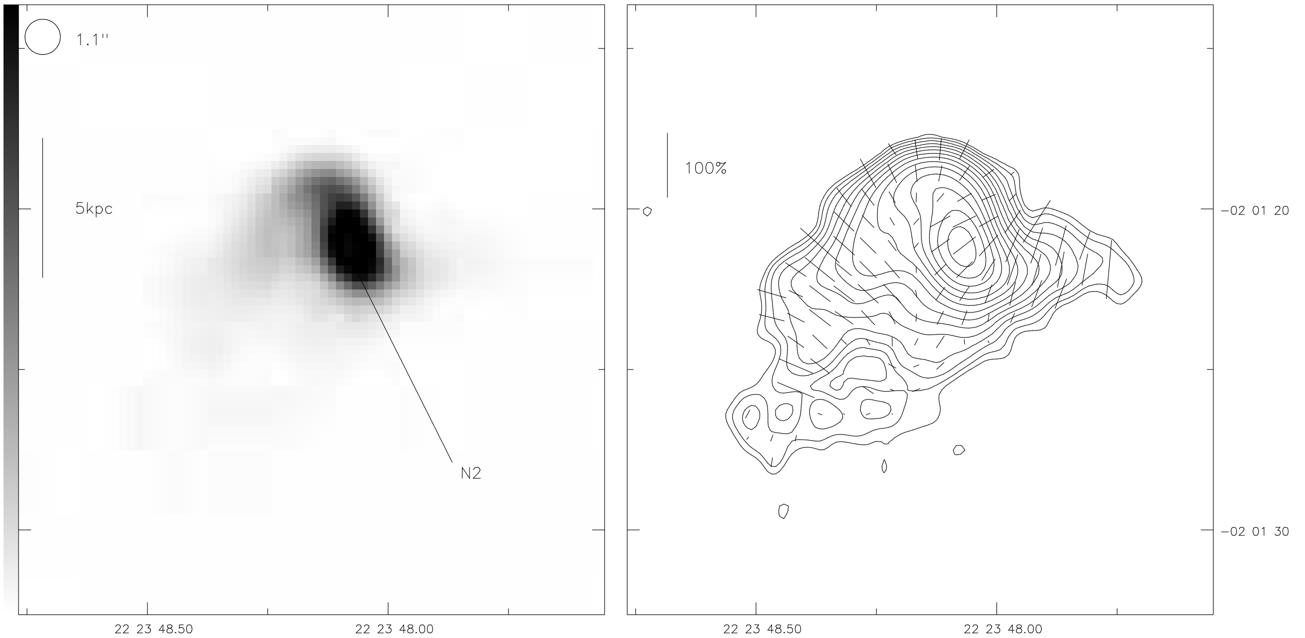

Figure 38. Np hotspot of 3C445 at 1.10 arcsec resolution. (a) Linear greyscale; black is 10 mJy beam^{-1}. (b) Contours at $0.15 \times (-\sqrt{2}, -1, 1, \sqrt{2}, 2, 2\sqrt{2}\ldots)$ mJy beam^{-1}. Negative contours are dashed.

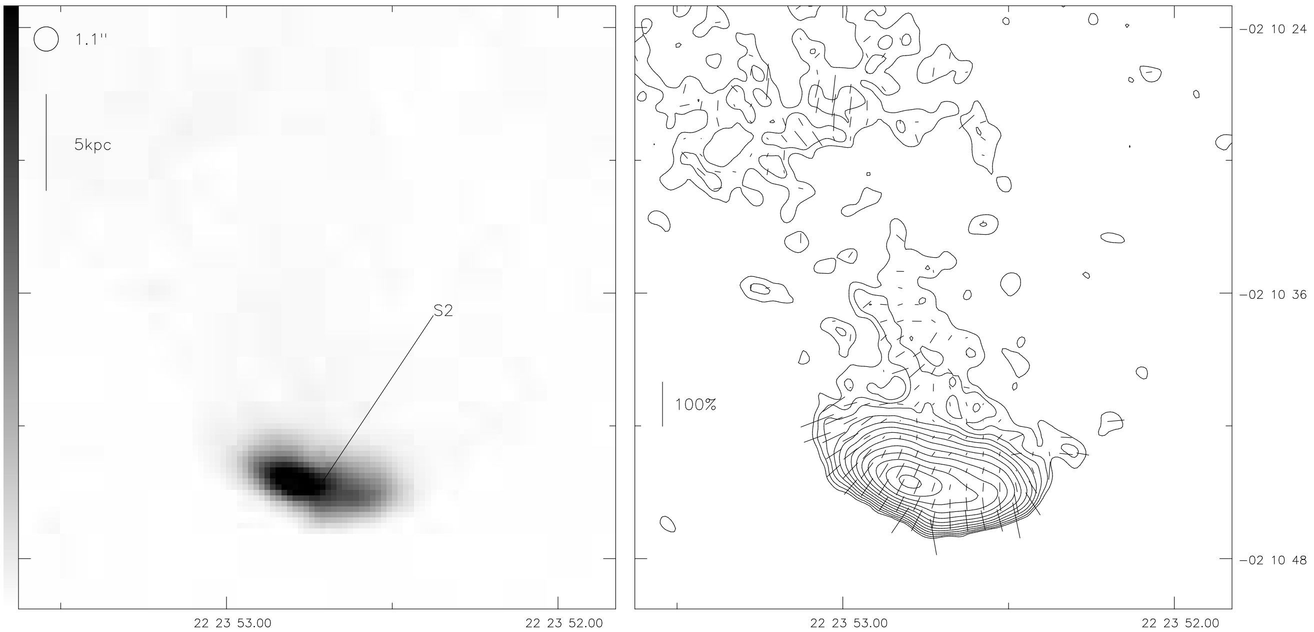

Figure 40. Sf hotspot of 3C445 at 1.10 arcsec resolution. (a) Linear greyscale; black is 10 mJy beam^{-1}. (b) Contours at $0.2 \times (-\sqrt{2}, -1, 1, \sqrt{2}, 2, 2\sqrt{2}\ldots)$ mJy beam^{-1}. Negative contours are dashed.

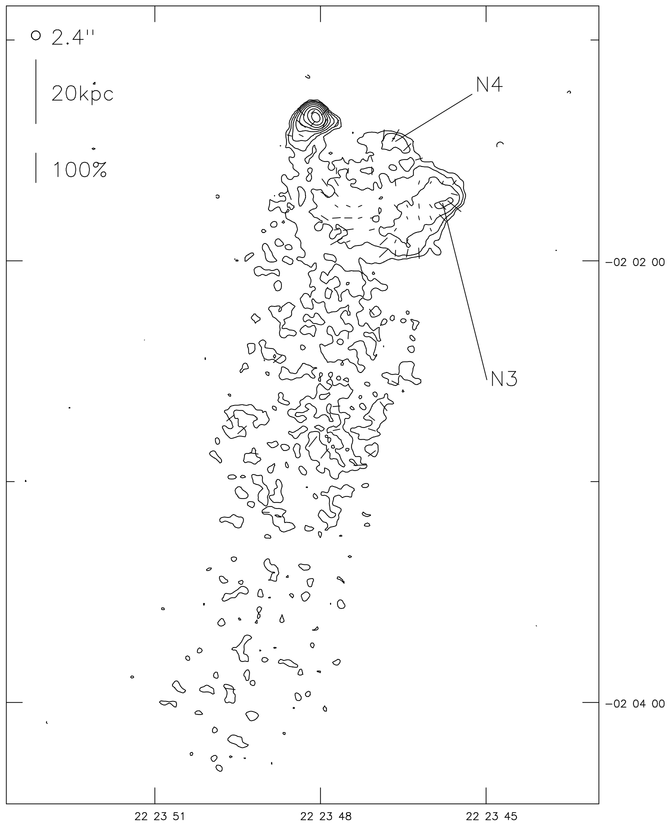

Figure 37. Np lobe of 3C445 at 2.40 arcsec resolution. Contours at $0.2 \times (-2, -1, 1, 2, 4, \ldots)$ mJy beam^{-1}. Negative contours are dashed.

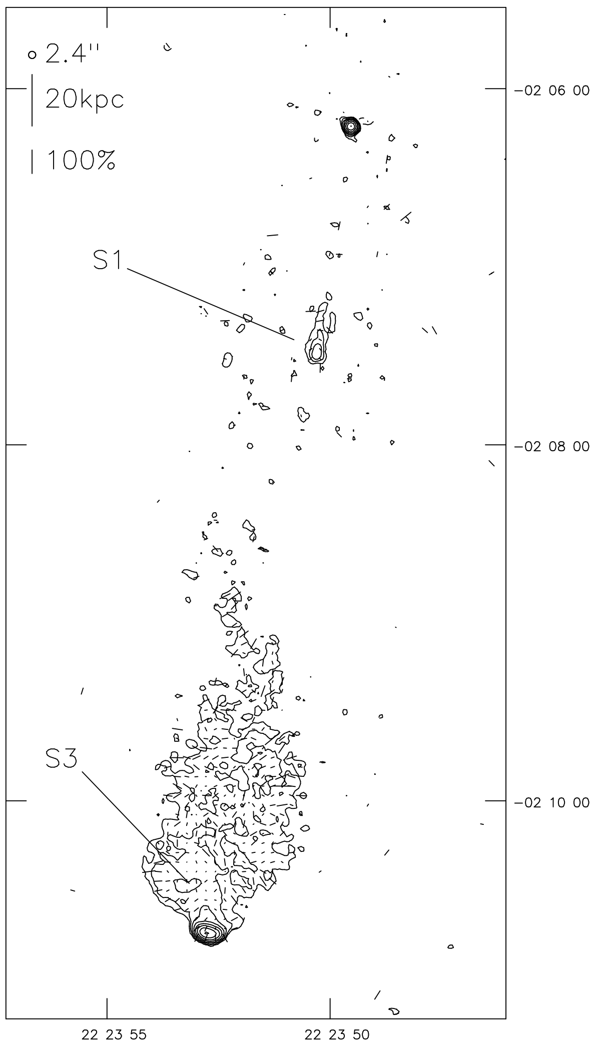

Figure 39. Sf lobe of 3C445 at 2.40 arcsec resolution. Contours at $0.25 \times (-2, -1, 1, 2, 4, \ldots)$ mJy beam^{-1}. Negative contours are dashed.